THE JOURNAL OF PHYSICAL CHEMISTRY C

Article

Proton Environments in Biomimetic Calcium Phosphates Formed from Mesoporous Bioactive CaO-SiO-PO Glasses *in vitro*: Insights from Solid-State NMR

Renny Mathew, Claudia Turdean-Ionescu, Yang Yu, Baltzar Stevensson, Isabel Izquierdo-Barba, Ana Garcia, Daniel Arcos, María Vallet-Regí, and Mattias Edén

J. Phys. Chem. C, **Just Accepted Manuscript** • Publication Date (Web): 23 May 2017

ACS Publications

The Journal of Physical Chemistry C is published by the American Chemical Society. 1155 Sixteenth Street N.W., Washington, DC 20036

Proton Environments in Biomimetic Calcium Phosphates Formed from Mesoporous Bioactive $CaO–SiO_2–P_2O_5$ Glasses *In Vitro*: Insights from Solid-State NMR

Renny Mathew[a,b], Claudia Turdean-Ionescu[a], Yang Yu[a], Baltzar Stevensson[a], Isabel Izquierdo-Barba[c,d], Ana García[c,d], Daniel Arcos[c,d], María Vallet-Regí[c,d], and Mattias Edén[a,*]

[a]Department of Materials and Environmental Chemistry, Arrhenius Laboratory, Stockholm University, SE-106 91 Stockholm, Sweden

[b]Present address: Department of Chemistry, New York University Abu Dhabi, Abu Dhabi, United Arab Emirates

[c]Departamento de Química Inorgánica y Bioinorgánica, Facultad de Farmacia, Universidad Complutense de Madrid. Instituto de Investigación Sanitaria Hospital 12 de Octubre i+12, 28040 Madrid, Spain; [d]Networking Research Center on Bioengineering, Biomaterials and Nanomedicine (CIBER-BBN) Madrid, Spain

*Corresponding author. E-mail: *mattias.eden@mmk.su.se*

Abstract

When exposed to body fluids, mesoporous bioactive glasses (MBGs) of the $CaO–SiO_2–P_2O_5$ system develop a bone-bonding surface layer that initially consists of amorphous calcium phosphate (ACP), which transforms into hydroxy-carbonate apatite (HCA) with a very similar composition as bone/dentin mineral. Information from various ^{1}H-based solid-state nuclear magnetic resonance (NMR) experiments were combined to elucidate the evolution of the proton speciations both at the MBG surface and within each ACP/HCA constituent of the biomimetic phosphate layer formed when each of three MBGs with distinct Ca, Si, and P contents was immersed in a simulated body fluid (SBF) for variable periods between 15 min and 30 days. Directly excited magic-angle-spinning (MAS) ^{1}H NMR spectra mainly reflect the MBG component, whose surface is rich in water and silanol (SiOH) moieties. Double-quantum–single-quantum correlation ^{1}H NMR experimentation at fast MAS revealed their interatomic proximities. The comparatively minor H species of each ACP and HCA component were probed selectively by heteronuclear ^{1}H–^{31}P NMR experimentation. The initially prevailing ACP phase comprises H_2O and "non-apatitic" HPO_4^{2-}/PO_4^{3-} groups, whereas for prolonged MBG soaking over days, a well-progressed ACP→HCA transformation was evidenced by a dominating O^{1}H resonance from HCA. We show that ^{1}H-detected ^{1}H→^{31}P cross-polarization NMR is markedly more sensitive than utilizing powder X-ray diffraction or ^{31}P NMR for detecting the onset of HCA formation, notably so for P-bearing (M)BGs. In relation to the long-standing controversy as to whether bone mineral comprises ACP and/or forms *via* an ACP precursor, we discuss a recently accepted structural core-shell picture of both synthetic and biological HCA, highlighting the close relationship between the disordered surface layer and ACP.

1 Introduction

Bone is a composite material consisting of platelets of Ca-deficient hydroxy-carbonate apatite (HCA) deposited on collagen-I fibrils, forming a complex hierarchical structure that underlies its extraordinary mechanical properties.[1,2] The very thin (2–10 nm) and elongated HCA platelets (30–50 nm long; 15–30 nm wide) pack themselves like a deck of cards, with the longest crystal axis aligned with the direction of the collagen fibril.[1–4] Besides minor amounts of non-collagenous proteins and glycosaminoglycans, bone comprises significant amounts of citrate (≈1 wt%) and water (≈10 wt%),[1,2,5] the latter associated with both the organic and inorganic components. While it is recognized that the H_2O content of bone is reduced on its ageing, which correlates with a loss of strength and stiffness, recent research suggests that the water and citrate components may have stronger bearings on the stability and mechanical properties of bone than was previously conceived, with their role of interfacing the stacked HCA platelets by acting like a glue that enhances the tissue strength.[5–9]

The OH content of bone mineral is significantly lower than for stoichiometric calcium hydroxyapatite (HA; $Ca_5(PO_4)_3OH$), which is the mother structure of biological/synthetic HCA. The deficiently of Ca^{2+}, PO_4^{3-} and OH^- species in biological apatite stems from various coupled ion substitutions that lead to incorporation of mainly HPO_4^{2-}, CO_3^{2-}, and F^- anions, together with cations such as Na^+, Mg^{2+}, and Sr^{2+}.[4,10] The element-specificity and high signal-sensitivity of magic-angle spinning (MAS) ^{1}H nuclear magnetic resonance (NMR) have been exploited in numerous investigations targeting the various proton ($\mathbf{H}_2O$, O$\mathbf{H}$, and $\mathbf{H}PO_4^{2-}$) species of bone mineral[6,11–14] and synthetic H(C)A,[6,15–22] as well as for unraveling the interfacing role of water between the HCA platelets.[6,8,9] Noteworthy, the mineral-associated ^{1}H and ^{31}P environments may be probed *selectively* by using cross-polarization (CP) MAS NMR experimentation utilizing interatomic ^{1}H–^{31}P distance-dependent heteronuclear dipolar interactions:[6,11–14,23,24] this allows for rejecting all

proton resonances from the organic components of bone/dentin that otherwise dominate ^{1}H NMR spectra recorded directly by single pulses. CPMAS-based NMR experimentation, such as the heteronuclear correlation (HETCOR) technique,[11,25] also enables the discrimination[8,23,24,26–28] of proton environments of amorphous calcium phosphate (ACP[29–31]) and crystalline H(C)A. Recently, several advanced heteronuclear NMR protocols have been applied for estimating the nm-scale organization and the extent of (dis)ordered domains in various heterogeneous phosphate-bearing materials, encompassing bone/dentin as well as synthetic composites.[7,8,16,17,23,24,32,33]

There are several NMR reports on the ^{1}H speciation in directly precipitated H(C)A[18–21] and as an integrated component in various synthetic multi-phase materials.[7,34] However, despite a vast literature on studies of HCA growth *in vitro* from biomaterials intended for bone/tooth implants, ^{1}H NMR studies targeting the *proton* environments in ACP and HCA generated *biomimetically* from such *substrate* biomaterials are very sparse.[26–28,35,36] One class of amorphous biomaterials is melt-prepared silicate-based *bioactive glasses* (BGs)[37] and their templated *mesoporous bioactive glass* (MBG) counterparts with an ordered mesopore arrangement:[38,39] when subjected to simulated body fluid (SBF), biomimetic HCA forms at the (M)BG surface *via* an ACP precursor,[26,27,37,40,41] as first proposed by Hench and co-workers.[37,40] *In vivo*, this biomineral-mimicking phosphate layer interfaces strongly with bone tissue.

A detailed insight into both the fundamental ACP/HCA formation mechanisms and the similarities/differences of the phosphate and proton speciations of biomimetic HCA and biological apatite is desirable. For three series of MBGs with variable Ca, Si, and P contents and SBF-exposure intervals ranging between 15 min and 30 days, we present a comprehensive MAS NMR study unveiling the evolution of the proton environments both at the MBG surface and within each ACP and HCA component of the growing biomimetic phosphate layer. The silicate and phosphate environments of the same set of specimens were previously characterized by ^{29}Si and ^{31}P MAS NMR;[42,43] those

findings are summarized in section **3**. They will be contrasted with the complementary information gained herein about the H species of the heterogeneous multicomponent specimens.

We provide results from single-pulse ^{1}H NMR and fast-MAS ^{1}H–^{1}H double-quantum–single-quantum (2Q–1Q) correlation NMR experiments, which inform primarily about the various water and silanol (SiOH) moieties and their interatomic proximities of the dominating H reservoir at MBG silicate surface, whereas the overall minor H populations of each ACP and HCA component of the phosphate layer were examined by heteronuclear ^{1}H–^{31}P NMR experimentation. The present work extends our previous ^{1}H NMR studies, which only discussed the surface proton speciations in detail for the *pristine* MBGs,[44] whereas the counterparts in SBF-soaked specimens were restricted to one MBG base composition and a limited number of exposure periods,[27,35] moreover involving a much higher MBG-loading in the SBF (20 g/L) than the current one (0.6 g/L).

The details of how bone mineral nucleates and to what extent this process is regulated by non-collagenous proteins and collagen remains unclear.[2,45–48] More remarkable is the long-standing controversy whether bone mineral is formed *via* transient precursor phases[2,4,10,45,46,49–51] of ACP and/or octacalcium phosphate[52,53] (OCP; $Ca_8(HPO_4)_2(PO_4)_4 \cdot 5H_2O$). Such a process is tempting, given the generally accepted feature that H(C)A forms *in vitro* by nucleation from an ACP phase[30,31,54]—and more precisely, *within* it[55–58]—as also demonstrated in a recent study of HA crystallization in the confined space of liposomes.[59] The discussions of the biomimetic HCA formation in our present and previous reports of SBF-exposed MBGs[27,28,42,43,60] adopt such an ACP→H(C)A conversion viewpoint. A detailed *in vitro*-mechanism was recently inferred by Habraken *et al.*,[56] showing that the embryos of "ACP" constitute prenucleation clusters of Ca^{2+} and HPO_4^{2-} ions, which subsequently evolve into HA *via* OCP–like phases.

However, despite early suggestions of ACP and OCP as precursors of biological apatite,[29,31,52,53] supported by a few recent bone and enamel mineralization studies in vertebrates,[61–64] an un-

refutable proof thereof have remained elusive,[2,45,46,50] leading to an alternative view that bone mineral crystallizes directly as tiny platelets of poorly ordered and highly ion-substituted HCA.[4,45,50,65] Nonetheless, recent insight on the structural organization of both synthetic and biological apatite involves a crystalline HCA core and a structurally disordered surface layer.[4,8,10,16,23,24,51,59,65–67] Expanding along the lines of refs.,[8,23,24] we argue that the latter is simply "ACP". A potential formation mechanism *via* an ACP precursor is then readily rationalized and the two *seemingly disparate* viewpoints may naturally be reconciled: this possibility—which generally seems to be overlooked in the literature—is commented in section **5.2** and will be discussed more thoroughly elsewhere (M. Edén, to be published).

2 Materials and Methods

2.1 MBG Preparation

Three MBG specimens of nominal molar compositions 10CaO–90SiO_2 ("S90"), 10CaO–85SiO_2–5P_2O_5 ("S85"), and 37CaO–58SiO_2–5P_2O_5 ("S58"), were prepared by an evaporation-induced self-assembly (EISA) procedure[68] at 40 °C, using the nonionic P123 triblock copolymer as structure-directing agent, and precursors of tetraethyl orthosilicate (TEOS), triethyl phosphate (TEP) and $Ca(NO_3)_2{\cdot}4H_2O$ to incorporate Si, P, and Ca, respectively. The detailed conditions are described in ref.[69] The resulting homogeneous membranes were heated at 700 °C for 6 h to remove nitrate ions and organic molecules. The textural properties and the experimentally determined cation compositions of the pristine MBGs are listed in Table **1**.

2.2 SBF-Exposed MBG Specimens

An SBF solution were prepared according to Kokubo *et al.*[70] by dissolving NaCl, KCl, $NaHCO_3$, $K_2HPO_4{\cdot}3H_2O$, $MgCl_2{\cdot}6H_2O$, $CaCl_2$, and Na_2SO_4 into distilled water. It was buffered at pH=7.38

by using tris(hydroxymethyl)-aminomethane/HCl (TRIS/HCl) and then passed through 0.22 μm Millipore filters to avoid bacterial contamination. 600 mg of a fine powder (<20 μm particle diameter) of each pristine MBG was immersed in 1.000 L of SBF in a sealed polyethylene container placed in an Ecotron HT incubator at 37 °C. The solutions were stirred at 100 rpm for each of the following periods: {0.25, 1, 4, 8, 24} h, and {3, 7, 15, 30} days. The solid phase was subsequently retained by filtration, soaked in acetone to quench the surface reactions, washed with water, and finally vacuum-dried at 37 °C for several days. The SBF-exposed specimens are henceforth denoted S90-τ_{SBF}, S85-τ_{SBF}, and S58-τ_{SBF}, with the immersion period τ_{SBF} specified either in hours ("h") or days ("d"). For example, S85-3d resulted by soaking the S85 MBG in SBF for 3 days (*i.e.*, 72 h). Prior to the NMR experiments, all samples were stored under dry conditions in a desiccator.

2.3 Solid-State NMR

The solid-state NMR experimentation was performed at external magnetic fields (B_0) of 9.4 T or 14.1 T, using Bruker Avance-III spectrometers operating at the respective ^{1}H Larmor frequencies of −400.1 MHz and −600.1 MHz. All single-pulse ("Bloch decay") ^{1}H NMR spectra were obtained at B_0 =9.4 T with 90° radio-frequency (rf) excitation pulses at a nutation frequency of $\nu_{\mathrm{H}} \approx 70$ kHz, and MBG/MBG-τ_{SBF} powders packed in either 4 mm or 7 mm ZrO_2 rotors undergoing MAS at the rate ν_r =7.00 kHz. The NMR acquisitions employed relaxation delays of 4.0 s and between 256–1024 accumulated signal transients. The NMR data of two polycrystalline HA powders (Aldrich) were recorded under similar conditions, except for using 4 mm rotors spinning at 14.00 kHz (16–64 transients).

^{1}H–^{1}H 2Q–1Q correlation NMR spectra were recorded from the S90 and S58-15d samples at B_0 =14.1 T, using 1.3 mm ZrO_2 rotors spinning at 66.00 kHz. Double-quantum coherences (2QC) were excited with two completed cycles of $[S\mathrm{R}2_4^1]$ (90°-pulse-sandwiched $\mathrm{R}2_4^1\mathrm{R}2_4^{-1}$)[71–73] with τ_{exc} =

$\tau_{\mathrm{rec}} = 242.4$ μs. The 2D NMR protocol shown in Fig. 1c of Teymoori *et al.*[72] was used, except that herein, 2QC were generated directly from longitudinal ^{1}H polarization. The ^{1}H nutation frequency was 33.00 kHz during dipolar recoupling and 125 kHz for all strong 90°/180° pulses. Rotor-synchronized 2QC reconversion was accomplished by a Hahn-echo lasting for two rotational periods between the excitation/reconversion events.[71,73] Both time-dimensions utilized rotor-synchronized time-incrementation, $\Delta t_1 = \Delta t_2 = 15.15$ μs, where $82(t_1)\times1024(t_2)$ time-points were acquired with 256 and 512 transients/t_1-value for S90 and S58-15d, respectively, and using 2.0 s relaxation delays. Each 2D grid was zero-filled to $512(t_1)\times8192(t_2)$ points and broadened by 120 Hz (sine bell shape) and 60 Hz (Lorentzian shape) along the 2Q and 1Q dimensions, respectively.

All heteronuclear ^{1}H–^{31}P CPMAS experiments were performed at 9.4 T, using 4 mm rotors spinning either at ν_r =14.00 kHz (2D HETCOR) or at ν_r =10.00 kHz when employing the ^{1}H-detected CPMAS protocol of Maltsev and Jäger,[17] which we will refer to as "*diffCP*" ("difference CP"). CP was established at the modified Hartmann-Hahn condition $\nu_{\mathrm{H}} = \nu_{\mathrm{P}} + \nu_r$, with the ^{31}P nutation frequency ramped around v_{P} = 40 kHz by ±1.5 kHz. The 90° ^{1}H pulse operated at v_{H} =78 kHz. The relaxation delays were 4.0 s. The contact interval (τ_{CP}) was 1.0 ms for the 2D HETCOR acquisition, whereas 0.2 ms or 6.0 ms were utilized for the diffCP counterparts, the latter typically averaged over 5000–24000 transients depending on the P content of the sample and the precise $\{\tau_{\mathrm{CP}}\,,\,\tau_{\mathrm{SBF}}\}$ values. The 2D HETCOR data was recorded with spectral windows of 56.0 kHz and 14.0 kHz for the direct ^{31}P and indirect ^{1}H spectral dimensions, respectively. 400 transients/t_1-value with $40(t_1)\times400(t_2)$ time-points were acquired and zero-filled to 256×2048 points.

^{1}H and ^{31}P chemical shifts are quoted relative to neat tetramethylsilane and 85% H_3PO_4(aq), respectively. All 2D NMR acquisitions implemented the States procedure[74] to yield absorptive peaks with frequency-sign discrimination along the indirect dimension, resulting in total 2D NMR

acquisition durations of 23 h (2Q–1Q; S90), 47 h (2Q–1Q; S58-15d), and 36 h (HETCOR; S85-1d). Despite using airtight rotors, the mechanical sample rotation during the NMR experimentation dehydrates the samples for experimentation over extended periods of days.

3 Previous Inferences about HCA Growth from MBGs

Before discussing the ^{1}H NMR results on the proton environments in the three series of S90-τ_{SBF}, S85-τ_{SBF} and S58-τ_{SBF} specimens, we review our main conclusions from complementary ^{31}P/^{29}Si NMR investigations on these samples.[42,43] The ACP formation and its conversion into HCA were quantified independently by powder X-ray diffraction (PXRD) and ^{31}P MAS NMR.[42] The results of the two characterization techniques agreed well: no significant HCA formation was detected by either method for immersion periods $\tau_{\mathrm{SBF}} < 24$ h, except for S90, where ^{31}P NMR revealed minor amounts of HCA already after 8 h. After 3 days of SBF soaking, roughly equal relative ACP:HCA fractions were observed for specimens of each S90, S85, and S58 series. Notwithstanding a net growth of ACP and HCA between 3–30 days, their *relative* fractions remained almost constant throughout, with the NMR and PXRD analyses yielding estimates of ≈50% and 60–80% of HCA, respectively, out of the total phosphate layer formed at any S90/S85/S58 MBG. It has been demonstrated that carbonate ions are present in both the crystalline and amorphous phosphate phases grown in SBF, implying that HCA forms rather than HA.[27]

Noteworthy, the HCA formation *rate* is essentially *independent* of either the precise {Ca, Si, P} MBG composition or the textural properties[42]—such as the surface area and pore arrangement, which differ among the S90, S85, and S58 specimens[39,42,69] (see Table **1**). This feature is likely to hold for *any* MBG *provided* that its surface area is *sufficiently large* ($\gtrsim$200 m^2/g); it was rationalized from the very similar silicate-reaction pathways observed for all three MBG structures, as inferred from ^{29}Si MAS NMR involving either direct excitation with single pulses or ^{1}H→^{29}Si

cross-polarization (CP):[43] after a rapid leaching of Ca^{2+}, which is completed within the first 15–60 minutes of SBF-soaking, essentially neat mesoporous silica remains that consequently degrades independently on the precise initial MBG surface area or pore arrangement.

As discussed in ref.,[43] the main distinction among the P-bearing S85 and S58 MBGs concerns how rapidly the structure is depleted of Ca and phosphate species, which may be rationalized from subtle distinctions in their structural roles: P is present as orthophosphate ions in amorphous calcium phosphate clusters (CaP) located in the pore-walls.[35,44,75] One fraction of the Ca reservoir charge-balances the PO_4^{3-} anions of the CaP clusters, while the remaining modifies the silicate network, whose Ca-associated silicate groups tend to accumulate near the pore-wall surface.[35,44] The latter portion only exists in Ca-rich (*e.g.*, S58) or P-free (*e.g.*, S90) MBGs, whereas essentially all Ca^{2+} species of the S85 structure are concentrated in the surface-associated and 1–2 nm-sized CaP clusters[75] that readily dissolve on their contact with aqueous solutions.[42,43,75] In contrast, the CaP clusters of the S58 MBG are much smaller and partly embedded *within* the silicate-network building the pore-wall,[75,76] thereby leading to a slower release of their Ca^{2+} and PO_4^{3-} constituents. The distinct CaP cluster scenarios are illustrated in Fig. 2 of Turdean-Ionescu *et al.*[43]

Notwithstanding the identical long-term dissolution behavior and nearly equal HCA formation *rates* manifested by the three S90, S85, and S58 MBGs, the *net amounts* of biomimetic ACP/HCA formed during SBF exposure indeed depends on the MBG composition:[42] they grow concurrently with the P content of the pristine MBG (see Table **1**). Hence, for a constant MBG mass (m_{MBG}) in a given SBF volume (V) and soaking period, the resulting amount of HCA increases according to S90<S85<S58.[42] This stems from a larger *total* P reservoir available from the MBG and SBF portions during the soaking of S58 relative to that of its P-free S90 counterpart. However, the property of essentially identical *in vitro* response-mechanisms from the three distinct MBGs *only* applies for SBF-testing under dilute conditions ($m_{MBG}/V \lesssim 1$ g/L).[42,43] Our early work employed

3–20 g/L;[27,28,35,60,69] such high MBG concentrations perturb the HCA formation by inducing an undesirable coupling between the MBG composition and the m_{MBG}/V ratio, leading to markedly retarded silicate-surface reactions and an impeded ACP→HCA crystallization (notably so for Ca-rich MBGs), as discussed in refs.[42,43,60]

4 Results

4.1 ^{1}H Speciations Probed by MAS NMR

A ^{1}H MAS NMR spectrum reveals the quantitative proton speciation of the heterogeneous MBG-τ_{SBF} specimen, which may comprise up to four distinct component phases, whose relative proportions depend on the SBF-soaking interval. The first two constituents are MBG-associated: (1) The silicate-based MBG pore-walls account for the largest proton reservoir, which predominantly consists of physisorbed water molecules and Si–OH moieties, regardless of the precise τ_{SBF}-value. (2) The MBG-associated amorphous CaP clusters comprise water and minor apatite-like OH groups.[28,44] However, this proton source is negligible and henceforth ignored, particularly because the CaP clusters readily dissolve on their contact with aqueous solutions (section **3**). The remaining proton-bearing phases are the (3) ACP and (4) HCA constituents of the phosphate layer growing at the MBG surface for increasing τ_{SBF}. Yet, these portions of the entire proton ensemble are minor and most of their ^{1}H NMR resonances are swamped by those from silanols and water; the selective probing of the phosphate-associated protons is discussed in section **4.3**.

Figure **1** displays a selection of ^{1}H MAS NMR spectra recorded from each series of SBF-exposed S90, S85, and S58 MBG samples, with τ_{SBF} increasing from top to bottom. All spectra reveal silicate surface-deriving resonances ($\gtrsim$ 2 ppm), as well some narrow signals (marked by asterisks), the most prominent ones appearing at 1.1 ppm and 3.6 ppm and stemming from C$\mathbf{H}_3$ and OC$\mathbf{H}_2$ groups. They originate mainly from remnant P123 block copolymers anchored at the pore-wall surface.[44]

Despite that they are minor, these resonances are emphasized by their narrow peak-widths (<30 Hz). These undesirable proton species are commented further in section **5.1** and onwards we focus on the targeted ^{1}H responses from the inorganic phases.

The precise ^{1}H chemical shift (δ_H) of each silicate/phosphate-associated O**H**/**H**$_2$O moiety is mainly dictated by its degree of hydrogen bonding to neighboring O atoms: the shift of an O**H**$\cdots$O fragment increases when the **H**$\cdots$O distance is decreased.[77,78] Hence, the globally *lowest* chemical shift ("most shielded ^{1}H") is manifested by the O**H** resonance from HCA, $\delta_H \approx 0.05$ ppm, where H-bonding is absent.[15] Naturally, this weak and broad peak is most pronounced in the NMR spectra from the MBG-30d specimens (Fig. **1**). Disregarding the HCA-associated ^{1}H shift and only focussing on the MBG-associated SiOH/H_2O ensemble, the lowest shift, $\delta_H \approx 1.85$ ppm, is observed from "isolated" SiOH groups devoid of H-bonding;[79,80] they are henceforth denoted $SiOH_{isol}$. They are present at *any* MBG surface (*e.g.*, see section **4.2**) but only produce clearly discernible ^{1}H resonances when the physisorbed water content is low. Consequently, the narrow resonance at $\delta_H \approx 1.85$ ppm is readily detected from each pristine MBG, but is not apparent after its exposure to the aqueous solution, owing to the substantial re-hydration and thereby emphasized H-bonding network among the various SiOH and H_2O moieties. All other ^{1}H NMR signals in the spectral region >2 ppm are relatively ill-defined for (moderately) high surface-hydration levels, due to a continuum of H-bonding scenarios and an accompanying NMR peak-broadening. Yet, three main groups of ^{1}H resonances may be identified in Fig. **1** and their relative contributions depend on the amount of surface-bound water:[44]

(*i*) ^{1}H resonances in the range of 2–4 ppm, which are signatures of a "dry" silicate surface, implying a minor water adsorption and thereby weakly H-bonded OH groups.[79–82]

(*ii*) A peak around 4.5–5 ppm that reflects physisorbed water and more extensively H-bonded SiOH groups.[44,80–82] This ensemble comprises two distinct portions, whose NMR signals are unre-

solved in the ^{1}H MAS NMR of Fig. **1**, but are distinguishable by other NMR features: the majority of the water pool is highly mobile, while the remaining (minor) portion is bound more tightly and may constitute the inner shell of the physisorbed species and/or water present as inclusions *within* the MBG pore-walls. The sizable ^{1}H–^{1}H through-space dipolar interactions (see section **4.2**) of the immobile species give spinning sidebands (not shown) at the modest MAS rate ν_r =7.00 kHz employed.[15,83,84] Yet, from the low sideband intensities relative to the centerband, we conclude that comparatively few H_2O molecules are immobile, whereas the dominant population do not produce sidebands but contribute to most of the centerband intensity in the spectra of Fig. **1**. The relative proportions of stationary and mobile water molecules depend on the precise surface hydration, but the latter portion dominates throughout (presumably $\gtrsim$ 80%).

(*iii*) Weak ^{1}H resonances in the high-ppm region ($\gtrsim$8 ppm) stem from strongly H-bonded species, encompassing minute contributions from acidic protons of HPO_4^{2-} anions of ACP[7,8,15–17,23,28] (see section **4.3**), but predominantly involving H-bonded SiO**H**$\cdots^-$OSi motifs, as observed from fragmented networks of hydrous silicate glasses comprising alkali/alkaline-earth metal ions.[83,84] Indeed, these NMR signals are only clearly discernible from the Ca-rich S58 MBG[35,44] and its S58-τ_{SBF} derivatives with short SBF-immersion periods up to ≈24 h; see Fig. **1**.

Noteworthy, the silicate-surface hydration and dehydration processes are reversible and the precise ^{1}H NMR peak position observed in the 3–5 ppm range reflects the given surface-water content when the NMR experiment was performed.[44,80–82] Despite that the ^{1}H NMR spectra presented herein were recorded on as-prepared samples stored in a desiccator prior to the NMR experiments, the quantitative proton speciations at the MBG surface is *not* an *intrinsic* sample property. Moreover, it is not possible to accurately control the amount of surface-associated water, because each S90/S85/S58 specimen (and its MBG-τ_{SBF} counterparts) exhibit *inherently distinct water affinities*: the degree of water adsorption enhances concomitantly with the Ca^{2+} population

at the MBG *surface*,[44] which increases according to S85$\lesssim$S90<S58 (where the surface-associated Ca^{2+} population is slightly higher for the P-free S90 structure relative to that of S85, whose entire Ca reservoir is present in the CaP clusters).[35,43] With these caveats in mind, we only discuss the gross trends of Fig. **1** concerning the evolution of the proton speciations of the various samples over the 30 days of SBF immersion, where we highlight the following:

(*i*) All pristine S90, S85, and S58 MBGs were heated at 700 °C (see *Materials and Methods*) and manifest relatively "dry" surfaces revealing ^{1}H NMR peak-maxima ≈ 4 ppm. On their SBF exposure, an enhanced surface hydration is evident for all MBG-0.25h specimens, as evidenced by the vanishing peak intensity ≈ 1.85 ppm from isolated silanols, accompanied by an overall resonance-broadening. The elevated population of surface-adsorbed water molecules is most evident for the Ca-richest S58-0.25h specimen, which additionally manifests an NMR peak-maximum displacement from ≈3.7 ppm (pristine S58) to 5.0 ppm, the latter typical for "liquid" $\mathbf{H}_2$O resonances.

(*ii*) For prolonged SBF-exposure of S90 and S85 (τ_{SBF} >24 h), the broad NMR peak gradually splits into two primary resonances that appear around 3.4–3.7 ppm and 5.0–5.4 ppm, suggesting two main "pools" of distinct proton environments that experience weak and moderately strong H-bonding, respectively (Fig. **1**). Overall, for a given τ_{SBF}-value, the S90-τ_{SBF} and S85-τ_{SBF} samples exhibit very similar NMR signatures, whereas the resonance from physisorbed water (≈ 5 ppm) is emphasized for the S58-τ_{SBF} surfaces, consistent with their higher water affinity.

(*iii*) In good qualitative agreement with the estimated HCA contents of Turdean-Ionescu *et al.*[42] (section **3**), the HCA-associated O**H** resonance (≈ 0 ppm) is clearly visible after SBF-soaking periods τ_{SBF} >24 h. Its intensity grows concurrently with both the SBF-immersion period and the P content of the MBG (Table **1**), *i.e.*, along the series S90<S85<S58, which becomes particularly evident when comparing the peak-intensity ≈ 0 ppm in the NMR spectra from S90-30d and S58-30d of Fig. **1**.

4.2 ^{1}H–^{1}H Proximities from Double-Quantum NMR

To qualitatively asses the spatial proximities among the various surface-associated proton species, we performed dipolar recoupling experimentation with the $[S\mathrm{R}2^1_4]$ pulse sequence[71–73] at ν_r=66.0 kHz. These experiments utilize *homonuclear* through-space ^{1}H–^{1}H dipolar interactions to excite 2QC, whose buildup rate reflect the dipolar-coupling magnitude in a pair of protons. This interaction depends on the inverse cube of the ^{1}H–^{1}H internuclear distance, but is also sensitive to molecular motions and averages to zero in the presence of rapid molecular reorientations. For instance, the ^{1}H–^{1}H dipolar interaction of the C$\mathbf{H}_3$/OC$\mathbf{H}_2$ groups of the residual polymers are motionally averaged, the extent of which depends strongly on the precise surface hydration level (and also underlying their varying NMR peakwidths among the spectra of Fig. **1**).

To identify *which pairs* of nearest-neighboring protons that exhibit "close" internuclear proximities ($\lesssim$ 0.5 nm), 2Q–1Q 2D NMR correlation spectra were recorded from the S90 and S58-15d samples for a short 2QC excitation interval of τ_{exc} = 242 μs. The 2D NMR spectrum from the pristine S90 MBG is displayed in Fig. **2**. A close proximity between two protons—resonating at the respective shifts $\delta^{\mathrm{A}}_{\mathrm{H}}$ and $\delta^{\mathrm{B}}_{\mathrm{H}}$ along the horizontal "1Q dimension" of the 2D NMR spectrum—is revealed by the presence of a 2D NMR signal at the corresponding 2QC shift, $\delta_{2\mathrm{Q}} = \delta^{\mathrm{A}}_{\mathrm{H}} + \delta^{\mathrm{B}}_{\mathrm{H}}$, which appears along the vertical "2Q dimension". A 2QC signal from two protons of the same type that feature equal chemical-shift values (δ_{H}) occurs at $\delta_{2\mathrm{Q}} = 2\delta_{\mathrm{H}}$, *i.e.*, along the diagonal of the 2Q–1Q spectrum marked by the dotted line in Fig. **2**. Incidentally, such "auto-correlation" signals dominate the 2D NMR spectrum from S90.

The 2Q–1Q NMR spectrum from the S90 MBG (Fig. **2**) is similar to our previous result from a pristine S85 specimen:[44] besides the narrow resonances at the 2QC shifts of 7.2 ppm and across 2–4 ppm that originate from 2QC among protons within each OC$\mathbf{H}_2$ and C$\mathbf{H}_3$ moiety, respectively, the primary signal represent a broad auto-correlation ridge associated with hydrogen-bonded SiO$\mathbf{H}$

groups. Yet, a correlation is also established among two $SiOH_{isol}$ sites at the surface, as is most evident from the slice along the 1QC dimension at δ_{2Q} = 3.8 ppm, shown to the right of the 2D NMR spectrum. The S90 surface hydration level was lower when the 2Q–1Q experimentation was performed relative to that giving the NMR spectrum of Fig. **1** (compare the directly excited spectra of Figs. **1** and **2**). Yet, considering that *most* silanols are weakly H-bonded (responsible for the overall largest NMR signal intensity ≈3.7 ppm), the shortest ^1H–^1H distance between two $SiOH_{isol}$ moieties is expected to be *longer* than that involving an isolated silanol (δ_H = 1.8 ppm) and a H-bonded ($\delta_H \approx$ 3.5 ppm) counterpart. Hence, the latter correlations should also be present: while they are obscured in the 2Q–1Q spectrum by the dominating auto-correlation ridge from pairs of H-bonded SiOH groups, those NMR signals appear in the slice at δ_{2Q} = 5.7 ppm as a broad resonance extending between 2–4 ppm and peaking at the shift of the $SiOH_{isol}$ group (Fig. **2**). There is also a 2QC auto-correlation involving the resonance at δ_H =4.8 ppm, whose origin is unknown; notwithstanding that both its chemical shift and narrow peak-width suggests physisorbed water, those mobile moieties should not permit 2QC excitation, as commented below.

The 2Q–1Q NMR spectrum obtained from S58-15d is displayed in Fig. **3**. It overall features the same correlations as those observed from S90, but differs primarily in two aspects. First, the SBF-exposed S58-15d specimen reveals an auto-correlation peak at zero ppm, originating from the O**H** groups of HCA. Second, the S58-15d powder was re-hydrated prior to the NMR experiments, as manifested by the absence of a significant spectral intensity from isolated silanols in the ^1H MAS NMR spectrum displayed in Fig. **3**, and by the prominent NMR peak at 5.1 ppm from mobile physisorbed water molecules. However, their motionally averaged ^1H–^1H interactions do not support 2QC excitation (see section **4.1**), as witnessed by the strong signal-intensity depletion $\gtrsim$4.5 ppm in the projection of the 2Q–1Q NMR spectrum of Fig. **3** relative to the Bloch-decay MAS counterpart. Noteworthy, fast-MAS experimentation at ν_r=66 kHz (Figs. **2** and **3**) does not

improve the NMR spectral resolution significantly relative to that ≈10 kHz (Fig. **1**) because the peak-widths are mainly dictated by chemical-shift dispersion rather than by homonuclear ^{1}H–^{1}H interactions.

Despite the higher surface hydration of S58-15d compared with S90, the 2Q–1Q NMR spectrum reveals that $SiOH_{isol}$ surface groups are present (Fig. **3**). Yet, as expected, their associated ^{1}H resonances are weaker and appear to mainly involve correlations with H-bonded silanols; see the slices extracted at δ_{2Q} =4.2 ppm and δ_{2Q} =5.7 ppm. Moreover, the larger population of H-bonded silanols is manifested in the 2Q–1Q spectrum by the auto-correlation ridge extending over a larger shift-range in both spectral dimensions (which is responsible for the "tail" towards higher shifts observed in the projection).

4.3 Phosphate-Associated Proton Environments

As follows from the hitherto discussed ^{1}H NMR results, only a minority of the ^{1}H resonances derive from the biomimetic ACP/HCA layer, most merely being associated with silanols and physisorbed water molecules at the MBG surface. Consequently, we performed ^{1}H→^{31}P CPMAS NMR experimentation for *selectively* probing the protons in close spatial proximity to phosphate groups of the heterogeneous calcium phosphate layer. Figure **4** displays a ^{1}H–^{31}P 2D HETCOR NMR spectrum recorded from the S85-1d sample. It informs *which* proton and phosphate species that are close in space by a pair-wise correlation appearing at the 2D coordinate $\{\delta_H, \delta_P\}$, with the chemical shifts of ^{1}H (δ_H) and ^{31}P (δ_P) being encoded along the vertical and horizontal dimensions of the 2D NMR spectrum, respectively. Each corresponding 2D spectral projection reveals a ^{1}H (vertical) and ^{31}P (horizontal) spectrum solely manifesting resonances that convey sufficiently strong ^{1}H–^{31}P contacts, with a "strong" ("weak") ^{1}H–^{31}P *contact* implying a short (long) ^{1}H–^{31}P internuclear distance and/or a higher (lower) number of protons in the vicinity of ^{31}P.

The ^{31}P projection in Fig. **4** exhibits a broad and nearly Gaussian peak at $\delta_P = 3.05$ ppm. It comprises three main components, all centered around nearly identical ^{31}P chemical shifts, as illustrated by the slices extracted at $\delta_H = \{0.0, 5.8, 12.0\}$ ppm from the 2D HETCOR NMR spectrum. One *narrow* ^{31}P NMR peak of full width at half maximum (fwhm) height of 1.94 ppm (315 Hz at $B_0 = 9.4$ T) is correlated with the narrow O**H** signal appearing at $\delta_H = 0.0$ ppm; it stems from the orthophosphate groups of HCA[27,28] that represents the well-crystalline "core" in the core-shell structural picture (see section **5.2**). All other ^{31}P NMR responses are significantly broader (fwhm 5.1–5.4 ppm) and correlate with ^{1}H shifts $\delta_H > 4$ ppm, all of which originate from ACP,[8,26–28,59] *i.e.*, the "hydrated HCA surface" in the core-shell view;[16,17,65,66] the most intense NMR peak at the shift-pair $\{\delta_H, \delta_P\} = \{5.8, 3.0\}$ ppm is assigned to "non-apatitic" PO_4^{3-} groups nearby water molecules, whereas the remaining correlations with $\delta_H \gtrsim 9$ ppm stem mainly from **P**–O**H** contacts in HPO_4^{2-} anions. These NMR responses account for the broad "tail" towards higher δ_H-values of the 2D HETCOR spectrum. Notably, they are not visible in the directly excited NMR spectra of Fig. **1**, underscoring that the ACP-associated H_2O and HPO_4^{2-} moieties are minute components of the *total* ^{1}H reservoir in any MBG-τ_{SBF} specimen. Yet, these strongly H-bonded species represent *all* protons around the phosphate groups in ACP,[8,16,17,23,28,59] which is devoid of the OH group constituting the fingerprint of well-crystalline H(C)A.

Figure **5** displays ^{1}H NMR spectra obtained from each S90, S85, and S58 MBG immersed in SBF for a short ($\tau_{SBF} = 4$ h) or long ($\tau_{SBF} = 30$ days) period, and acquired either by single pulses ("1pls"), or by the "diffCP" protocol.[17] The latter yields a ^{1}H NMR spectrum solely comprising the resonances from protons involved in magnetization transfers to neighboring ^{31}P sites in *one* 1D NMR acquisition.[17] Hence, the diffCP-derived NMR result is identical to the projection along the ^{1}H dimension of a ^{1}H–^{31}P HETCOR NMR spectrum, but it circumvents the time-consuming 2D NMR acquisition. diffCP NMR is also strongly preferred over ^{31}P→^{1}H CPMAS application,[14,85,86]

which is plagued by much slower T_1 relaxation than the reverse ^{1}H→^{31}P process. As expected, all NMR spectra of Fig. **5** reveal *at least* one of the ^{1}H resonances observed in the projection of the HETCOR NMR spectrum: a narrow peak at 0 ppm from the O**H** groups of HCA, and responses from $\mathbf{H}_2$O (peaking ≈5 ppm) and $\mathbf{H}PO_4^{2-}$ anions (≈12 ppm).

The ^{1}H–^{31}P diffCP NMR experiments involved magnetization transfers activated over both short (τ_{CP} = 0.2 ms) and long (τ_{CP} = 6.0 ms) periods, thereby enabling a qualitative proximity probing over "short" ($\lesssim$ 0.3 nm) and "longer" ($\lesssim$ 1 nm) ^{1}H–^{31}P distances, respectively. As discussed previously,[28] the overall stronger ^{1}H–$^{31}PO_4$ contacts of ACP relative to HCA are mirrored in its NMR signal being maximized already at τ_{CP} ≈ 1.5 ms, whereas the HCA counterpart exhibits a slower but continuous growth for increasing contact periods, reaching a plateau around 6 ms. Overall, the most rapid magnetization transfers occur across the **P**–O**H** fragments of HPO_4^{2-} groups:[16] this accounts for the generally emphasized high-ppm intensities in the diffCP-derived data of Fig. **5** that utilized τ_{CP} = 0.2 ms, as compared with the ^{1}H–^{31}P HETCOR counterpart of Fig. **4** that employed a longer contact period of 1.0 ms and thereby favoring the $\mathbf{H}_2O/\mathbf{P}O_4^{3-}$ pair.

Consequently, utilizing a short contact interval of 0.2 ms emphasizes the ^{1}H NMR responses from the amorphous phase(s) and enables their (near) selective probing. This is evident from Fig. **5**: *regardless* of the τ_{CP}-value, all NMR results for the MBG-4h samples stemming from a short SBF-exposure interval reveal predominantly resonances from ACP. Yet, the very weak O**H** peak-intensity ≈ 0 ppm observed for τ_{CP} = 6.0 ms evidences a minute HCA formation already at this short incubation period (see section **5.4**). Moreover, the nearly complete *selective* excitation of the ^{1}H NMR signals from ACP is manifested by *all* NMR spectra acquired with τ_{CP} =0.2 ms from the MBG-30d specimens, which comprise *both* ACP and HCA (Fig. **5**). For the MBG-30d samples, all NMR data recorded by employing the longer contact period (τ_{CP} = 6.0 ms) reveal mainly the narrow O**H** signal from HCA, because relaxation processes during CP damp the ACP-stemming

resonances even over short contact intervals of a few ms.[16,17,28]

Besides the targeted $^{1}H \rightarrow ^{31}P$ magnetization transfers from the protons of the ACP/HCA components, weak transfers *also* occur from those of the organic templating molecules; they are most pronounced for the MBG-4h specimens for $\tau_{CP} = 6.0$ ms. We consider these signals as artefacts that might have leaked through the phase-cycle, although their emphasized intensities consistently observed for the *longer* contact interval of 6.0 ms may indeed reflect transfers from the aliphatic surface-anchored organic moieties to the surrounding ACP phase growing at the pore surface.

5 Discussion

5.1 Origin of the ^{1}H signals around 1 ppm?

The narrow resonances at 0.8 ppm, 1.1 ppm, and 1.3 ppm observed in ^{1}H NMR spectra from the MBG and MBG-τ_{SBF} samples (Figs. **1**–**3**, **5**) are doubtlessly of *organic* origin. Besides the results herein, we refer to Leonova *et al.*[44] for detailed assignments and further discussions. Concerning ^{1}H NMR characterizations of the already complex systems of mesoporous silica co-existing with its heterogeneous surface layer of calcium phosphates, these NMR peaks are a nuisance and may lead to assignment ambiguities—even as to the precise *organic source* molecules, as shown below. However, these NMR signals are worth discussing in more depth because similar (but distinct) NMR responses are frequently observed across the shift-range 0.8–1.4 ppm from apatites, encompassing HA,[13–16,22] HCA,[6,13,14,19–21] fluoro-hydroxyapatite[15,87] as well as bone mineral.[6,13,14] These resonances are usually very weak from *well-crystalline* HA, as may be verified from the ^{1}H NMR spectra of Fig. **6**(a, b).

First focussing on the minor ^{1}H resonances from synthetic H(C)A, their precise shifts and intensities vary slightly among samples and studies, but (at least) two peaks are reported around 0.8–0.9 ppm and 1.2–1.4 ppm, respectively,[6,13–16,21,22] occasionally accompanied by another res-

onance around 2.0 ppm.[14,21] Their narrow peakwidths ($\lesssim$30 Hz) and absence of magnetization transfers in ^{1}H–^{31}P CPMAS-based experimentation suggest species that are either highly mobile and/or remote from phosphate groups.[14,16] Furthermore, the peak intensities grow concurrently with the surface area of the H(C)A crystallites and are most pronounced for *nano*-crystalline HA powders.[16] Altogether, these characteristics point towards surface-associated species whose populations depend on the surface hydration level,[21] but unambiguous assignments have until recently remained elusive. Similar narrow peaks are also observed from HCA with significant carbonate-for-phosphate substitutions ("B-type" HCA),[13,18–21] where they have been attributed to O**H** groups close to CO_3^{2-} ions.[6,13,18,19]

The hitherto most convincing solution to the enigma of the origin of the narrow NMR responses in the 0.8–1.4 ppm range—at least for well-ordered HA—was recently provided by Ben Osman *et al.*,[22] who applied a suite of characterization protocols to HA samples with controlled (but relatively low) surface hydration levels. All ^{1}H resonances appearing at {0.8, 1.1, 1.3} ppm were attributed to H_2O molecules that terminate the OH channels (which are aligned with the *c* axis of the crystal frame). The 1.1 ppm signal dominates for higher amounts of surface-bound water; its intensity is reduced on drying, whereupon two peaks at 0.8 ppm and 1.3 ppm emerge, which were assigned to H_2O molecules oriented "up" and "down" relative to the O**H** groups in the channels, respectively.[22] However, it is unlikely that the assignments of ref.[22] account for the significantly more intense ^{1}H resonances $\approx$1 ppm observed from OCP, which have been tentatively attributed to mobile H_2O molecules.[9,15] Noteworthy, similar signals at {0.8, 1.1, 1.2} ppm reported by Souza *et al.* from biomimetic HCA (generated by exposing melt-prepared BGs to SBF) were assigned to a poorly ordered OCP-like precursor of HCA.[36]

Yet another potential source for ^{1}H NMR signals $\approx$1.1 ppm is C**H**$_3$CH$_2$OH, which may arise from incompletely dried HA powders washed in ethanol.[20] Indeed, after soaking the "HA-2" powder

in ethanol, three narrow peaks at {0.88, 1.10, 1.30} ppm are observed (Fig. **6**(c); red trace), incidentally at shifts indistinguishable from those we assigned to remnant templating molecules in Fig. **1**, *as well as from* those discussed by Ben Osman *et al.* in the context of HA.[22] The sole, yet decisive, distinction to the H(C)A/OCP-associated ^{1}H resonances is the accompanying peak at 3.64 ppm from the OC$\mathbf{H}_2$ group of ethanol [Fig. **6**(c)], which together with the intense signal at 1.10 ppm derives from bulk liquid ethanol. The much weaker responses at 0.88 ppm and 1.30 ppm, on the other hand, are attributed to strongly physisorbed ethanol molecules at the HA surface: notably, the latter intensities remained almost unaffected on removal of the HA powder from the rotor, followed by its immediate repacking and subsequent NMR acquisition (black trace), whereas the intensity at 1.10 ppm diminished markedly by evaporation of the liquid. Moreover, two very weak signals at 2.04 ppm and 1.60 ppm (with essentially unaltered intensities) are observed in both spectra of Fig. **6**(c). They may originate from non-volatile impurities of the ethanol batch.

5.2 The Disordered Phosphate Component: ACP or Apatite Surface Layer?

A "core-shell" structural model, involving a crystalline HCA core and a disordered surface layer rich in "non-apatitic" HPO_4^{2-} moieties, has been proposed and discussed in the literature.[4,10,50,51,65–67] Recently, this structural picture of H(C)A appears to be well accepted, partially thanks to the recent and detailed NMR-derived constitution of both synthetic H(C)A and biological apatite:[8,16,23,24] besides the Ca^{2+} constituent of *both* core-shell components (and CO_3^{2-} in the context of HCA), the model involves an ordered H(C)A *core* of "apatitic" PO_4^{3-} and OH^- ions, and a *disordered surface layer* comprising water and "non-apatitic" HPO_4^{2-} and PO_4^{3-} moieties, as illustrated in Fig. 7(**a**).

Unfortunately, different nomenclatures encountered in the literature concerning the "hydrated surface layer" and "ACP" obscure their strong similarities, thereby implicitly highlighting their distinctions. Nevertheless, common to all recently reported (approximate) HCA-surface composi-

tions[8,16,23,24] is the presence of HPO_4^{2-} and H_2O species, a feature *also shared* with both OCP[9,15] and recently deduced compositions of ACP.[56,57] Moreover, the demonstrated *variable* H_2O contents in both ACP and the surface layer of synthetic/biological HCA[8,65] imply an *inherently non-unique* chemical speciation that depends on the precise surface hydration level. The ^1H–^{31}P HETCOR data of ref.[8] obtained from both synthetic HCA and sheep bone are consistent with a "dry" and "wet" HCA surface reflecting a comparatively enhanced contribution from HPO_4^{2-} and PO_4^{3-}/H_2O species, respectively. (Analogously with the direct dependence of the ^1H speciation at the MBG silicate surface on its hydration level; see section **4.1**). Likewise, the ^1H–^{31}P HETCOR NMR spectra monitoring the transformation between disordered/HA phases in liposomes[59] are readily rationalized by ACP incarnations with variable H_2O/HPO_4^{2-} contents as the crystallization progressed (compare with the results by Wang *et al.*[8]). On the basis of different ^1H–^{31}P CPMAS parameters, Chen *et al.*[59] deliberately chose the nomenclature "disordered phosphate" to highlight its distinction to "ACP" obtained directly by precipitation. Nonetheless, it may be too early to dismiss its identification with ACP, where we also note that distinct and sequential "ACP-1" and "ACP-2" precursors of HA are discussed in the literature (*e.g.*, see refs.[54,57]).

Furthermore, despite careful and sensible analyses,[7,8,16,23,24] the non-quantitativeness of the NMR experimentation invoked for discriminating and estimating the various proton/phosphate populations in the "core" and "surface" apatite domains imply relatively large uncertainties that merit caution in claiming precise compositions. The hurdles of precisely quantifying the relative PO_4^{3-}, HPO_4^{2-}, and H_2O contents of "ACP" and "OCP-like" phases, coupled with the *nonetheless similar* compositions reported for the H(C)A surface portion,[8,16,23,24,65] suggest that "ACP" is a good approximant and that it may be premature to make too categorical statements when describing the nature of the H(C)A surface layer, as well as the "disordered calcium phosphate" phase observed in liposomes.[59] With one notable exception,[8] the H(C)A surface layer is in general *not* identified

explicitly as "ACP".[4,10,16,50,65] Moreover, adopting a looser terminology of "disordered OCP", would better bring out its structural similarity with both ACP and the H(C)A surface layer.

Concerning the issue of "separate HCA and ACP components" or an "HCA core and a disordered surface layer", one must distinguish the aspects of (*i*) the core/surface parts of each *individual* HCA particle [Fig. **7**(**a**)] from (*ii*) a distribution of such *particles* with *variable* surface and core volume fractions [*i.e.*, an ensemble of particles with varying degrees of crystallinity; see Fig. **7**(**b**)], yet noting that they are *in general correlated*. For instance, since the crystallization of *in vitro*-formed HCA starts *within* the ACP phase,[55–58] its interior will have a comparatively higher fraction of crystallites where the "HCA core" dominates over its surface (ACP) portion, while the latter prevails in the outer parts of the bulk; see Fig. **7**(**c**). This relates to the inferences of Beniash *et al.*,[62] who attributed the "outer" and "inner" parts of mouse enamel as ACP and HCA, respectively. However, their interpretation did not refer specifically to the core/surface of *individual* HCA crystallites but merely to large collections thereof probed over a 10^2–10^3 nm scale. Likewise, the rat dentin model proposed by Chan and co-workers[23,24] was discussed in terms of inner (HCA) and outer (ACP) portions.

Which most naturally adopted viewpoint of an "ACP phase" or an "apatite surface-layer" depends on the relative amounts of crystalline and amorphous material, where we here also comment on our interpretations in the context of the biomimetic *phosphate layer* of the MBG-τ_{SBF} specimens: In the limit of a negligible apatite core, *i.e.*, when the volume of the HCA surface layer vastly dominates, it seems most reasonable to view the particle ensemble as an ACP phase co-existing with a low number of small apatite crystallites [Fig. **7**(**c**)]; this applies for MBGs immersed in SBF for periods τ_{SBF} <24 h, where the specimen remains XRD-amorphous and the HCA ("core portion") is very minor. In contrast, for more mature nanocrystalline H(C)A/bone mineral with the surface layer accounting for $\lesssim 50\%$ in volume[16,24]—relevant for the present MBG-τ_{SBF} specimens

with $\tau_{SBF} \geqslant 3$ days[42]—the core-shell picture may be most suitable [Fig. **7**(**d**)], yet with the identification of the "surface layer" as "ACP", the latter taken to encompass a range of chemical compositions.[8] Furthermore, the "surface layer" observed for nano-crystalline HCA particles is *absent* for well-ordered and μm-sized HA crystals prepared *in vitro* by precipitation followed by heat treatment;[8,16,22] see Fig. **6**(a) for the ^{1}H signatures of such a specimen. This feature may be viewed as a complete ACP→HA conversion.

Worth highlighting is that once an *equivalence* between the HCA surface layer and ACP is accepted, the controversy of ACP being a component of (mature) bone mineral is settled, while it also becomes (even) more plausible that ACP would indeed be a precursor of biological apatite. Notably, this *reconciles* the viewpoints that "ACP precedes HCA formation" or "small and poorly ordered HCA particles form directly", which are simply two sides of the same coin, with their seeming differences becoming semantic.

5.3 Proton Environments of *In Vitro*-Grown ACP and HCA

The ^{1}H NMR data of Fig. **5** corroborates our earlier inferences from ^{31}P NMR about a dominance of ACP after 4 h of SBF exposure, whereas both ACP and HCA co-exist after 30 days of MBG-exposure to SBF.[42] The ^{1}H–^{31}P results of Figs. **4** and **5** accord overall with our previous ^{1}H–^{31}P HETCOR 2D NMR spectra[27,28] from SBF-soaked S85 specimens that feature very similar analyzed cation compositions as the present one, as well as those reported for synthetic nanocrystalline H(C)A specimens and bone/dentin.[6,8,13,16,23,24]

However, there is one notable distinction to our earlier results: ^{1}H resonances from acidic protons were *not* observed and structural water represented the *sole* proton reservoir of ACP.[27,28] The signal-to-noise ratios (S/N) of the present NMR data (notably so the ^{1}H–^{31}P diffCP NMR spectra) are significantly higher than that of our previous ^{1}H–^{31}P HETCOR results, suggesting

that the broad resonances in the high-ppm spectral region might have escaped detection. This is, however, unlikely considering that the $\mathbf{H}_2O$ NMR peak was readily observed,[27,28] implying that the ^1H resonances from acidic sites should also have been detected, *if present* in comparable water/acidic proportions as those revealed in Figs. **4** and **5**. More probable is that the ACP component of our present SBF-exposed MBG specimens comprise significantly higher amounts of HPO_4^{2-} populations (except for S90-4h, see Fig. **5**).

The apparently distinct ACP compositions could potentially stem from the more dilute MBG loading employed in our current SBF testing relative to that of previous reports, which altered the reactions at the MBG surface and thereby also the HCA growth[42,43,60] (section **3**). However, considering that the precise ACP composition depends on the net hydration level[8] (section **5.2**), it is more likely that the biomimetic phosphate layers of the present MBG-τ_{SBF} specimens were less hydrated than the previous ones (refs.[27,28]). This readily rationalizes that the amount of acidic protons is emphasized relative to that of H_2O molecules after 30 days of SBF immersion compared with the ACP phase formed after 4 h, as follows by contrasting the ^1H–^{31}P diffCP NMR results ($\tau_{CP} = 0.2$ ms) of Fig. **5** for the short and long SBF-soaking periods.

At a fixed τ_{SBF}-value of either 4 h or 30 days, the ^1H speciation of each biomimetic ACP/HCA component is almost independent on the precise {Ca, Si, P} composition and textural properties of the MBG (Table **1**), thereby confirming the equal suitabilities of S90/S85/S58 for acting as a substrate for the HCA growth. The main distinction observed among the diffCP-derived ^1H NMR spectra in Fig. **5** is the absence of signals from acidic protons in the S90-4h specimen. Overall, the significant shift-dispersion for all $\mathbf{H}_2O/\mathbf{H}PO_4^{2-}$ resonances from ACP reflect highly disordered ^1H environments. Yet, some ordering tendencies are evident from the ^1H NMR spectra of the MBG-30d specimens relative to their MBG-4h counterparts ($\tau_{CP} = 0.2$ ms): at the longer SBF-immersion period, a well-defined NMR-peak maximum ≈ 12 ppm is observed for the

$\mathbf{H}PO_4^{2-}$ resonances. Incidentally, this shift accord with that around 12–13 ppm reported for the acidic protons of OCP,[9,11,15] suggesting "disordered OCP" environments. The S85-30d sample additionally manifests a very weak and sharp peak at δ_H =10 ppm, indicating a minute brushite ($CaHPO_4 \cdot 2H_2O$) formation.[11–13,15] Moreover, while the biomimetic HCA phase in the MBG-30d specimens is classified as "crystalline", a remaining structural disorder—partly stemming from incorporation of CO_3^{2-} and Na^+ ions[27]—is mirrored in the fwhm ≈1.0 ppm of the O**H** resonance (Fig. **5**) relative to that ≈0.4 ppm observed from well-ordered HA crystallites (Fig. **6**).

5.4 Detecting the Onset of HCA Formation: ^{1}H *versus* ^{31}P NMR

The reduced experimental time offered by ^{1}H–^{31}P diffCP-MAS NMR experimentation, relative that of arranging a full 2D HETCOR or ^{31}P→^{1}H CPMAS NMR spectrum, suggests that diffCP is an attractive alternative for detecting the *onset* of HCA formation, besides the standard techniques of using infrared spectroscopy, PXRD, or electron microscopy, as well as the more recently introduced option of deconvoluting single-pulse ^{31}P MAS NMR spectra.[27,88] Noteworthy, the clearly discernible HCA-associated O**H** resonance observed from *each* S90-4h, S85-4h, and S58-4h samples (Fig. **5**) unambiguously evidences that a minute but non-negligible HCA formation occurred already after 4 h of SBF exposure. This may be contrasted with the failure of PXRD to detect HCA from any of the present MBG specimens with τ_{SBF}<24 h. The same conclusion was reached by ^{31}P NMR, except that the P-free S90 MBG revealed HCA after 8 h of SBF exposure.[42] The O**H** resonance intensity (Fig. **5**; τ_{CP} = 0.2 ms) grows along the series S90<S85<S58, in accordance with the results of Fig. **1** that corroborates our previous conclusion from ^{31}P NMR.[42]

The discrepancy with ^{31}P NMR—which suggested a *shorter* HCA induction period of 8 h from the S90 MBG relative to 24 h for S85 and S58[42] (in contrast with the ^{1}H NMR data herein)—stems partially from interferences of broad ^{31}P resonances from remnants of the amorphous CaP clusters

of the pristine S58/S85 MBG structures: while they dissolve readily into the aqueous medium, this process is likely not completed until ≈8–24 h (and is slower for S58 relative to S85[42,43]). The quantification of each biomimetic ACP and HCA component by ^{31}P NMR relies on the overall peak-narrowing accompanying the ACP→HCA transformation and a deconvolution of the ^{31}P NMR signal into two components, one broad from ACP and one narrow from HCA, both of which overlap and are centered around the same ^{31}P chemical shift (3 ppm);[27,42,60] see Fig. **4**. However, the ^{31}P NMR signals from the disordered CaP clusters are essentially indistinguishable from the SBF-induced ACP component.[27,28,42] Consequently, *if* they are present *together*, the (as-assumed sole) ACP content becomes overestimated, with the CaP-stemming ^{31}P resonances obscuring the detection of the narrow ^{31}P counterpart from HCA: the absence of broadening of the *net* NMR peakshape from the presence of the CaP clusters most likely enabled the detection of HCA from the *P-free* S90 specimen already after 8 h in SBF, notwithstanding that *larger* amounts of HCA are formed from the *P-bearing* S85 and (particularly) S58 MBGs over longer exposure periods,[42] as commented above. Consequently, another factor contributing to the apparently delayed HCA generation from the S85/S58 MBGs is the presence of *higher* amounts of ACP formed from the P-bearing MBGs, accompanied by a larger contribution of broad ^{31}P resonances.

Fortunately, the *undesirable* CaP-stemming NMR signals are *absent* when exploiting ^{1}H NMR, although the inherently non-quantitative nature of CPMAS-based experimentation makes accurate quantifications cumbersome. Hence, once the HCA formation is significant, we recommend single-pulse ^{31}P NMR for quantifying the relative ACP/HCA fractions; we guide the reader to refs.[42,60] for discussions on the relative merits of PXRD and ^{31}P MAS NMR for detecting and quantifying the relative and absolute ACP/HCA amounts. We stress that in the core-shell HCA picture (section **5.2**), the "HCA fraction" deduced from ^{31}P NMR reflect the *well-ordered core* of the HCA particles, whereas for an essentially complete ACP→HCA conversion, the "ACP fraction" is best interpreted

as the volume fraction of the disordered *surface* of the HCA crystallites.

6 Conclusions

We have examined the various H species present at the surfaces of three pristine MBGs, as well as in the silicate/phosphate portions of the heterogeneous MBG-τ_{SBF} specimens resulting after immersing each MBG in SBF for variable periods up to 30 days.

^{1}H NMR spectra recorded by single pulses are dominated by resonances from the MBG surface, encompassing two distinct pools of physisorbed water molecules: a main population of mobile species and a minor ensemble that is more strongly surface-bound; their precise amounts are difficult to quantify and depend on the overall surface hydration level. The MBG surface is also rich in SiOH moieties that exhibit variable degrees of H-bonding, distinguished by their ^{1}H chemical shifts, where three co-existing proton species were identified: those of (*i*) "isolated silanols" devoid of H-bonding, and those experiencing (*ii*) weak and (*iii*) strong H-bonding. Their relative abundances depend on the MBG-surface hydration level, where weakly H-bonded SiOH groups are most common at surfaces of the Ca-poor (pristine) S90/S85 MBGs and their MBG-τ_{SBF} counterparts resulting from *extended* SBF-soaking periods beyond 24 h. For short SBF-exposure intervals within a few hours, on the other hand, a higher surface hydration level is manifested both by the (near) absence of isolated SiOH groups and an overall resonance broadening. Protons of the strongest H-bonded motifs, such as Si$\mathbf{O}$H$\cdots^{-}$OSi, are only observed in the fragmented silicate networks of the Ca-rich—and thereby most hydrophilic—S58 MBG surface and its SBF-soaked counterparts. 2Q–1Q correlation ^{1}H NMR experiments revealed predominantly auto-correlations among the H-bonded Si$\mathbf{O}$H/$\mathbf{H}_2$O moieties, as well as between pairs of isolated silanols.

In directly excited ^{1}H NMR spectra, resonances from the minor ACP/HCA components are generally swamped by those from their MBG counterparts. Nevertheless, over days of SBF-

soaking, the HCA-characteristic O**H** signal (≈0 ppm) is clearly discernible. Its intensity grows concomitantly with the soaking period and the P content of the (pristine) MBG, *i.e.*, along the series S90<S85<S58, thereby corroborating the HCA-formation trends deduced by ^{31}P NMR from the same specimens.[42] Yet, an accurate probing of the minor H speciations of the biomimetic ACP/HCA components of the MBG-τ_{SBF} specimens is best performed with heteronuclear ^{1}H→^{31}P CPMAS-based experimentation, which revealed distinctly different ^{1}H reservoirs of the amorphous and crystalline phosphate portions: the latter comprises solely OH groups, whereas ACP incorporates water and acidic protons of HPO_4^{2-} anions. Besides the strong **P**–O**H** contacts within HPO_4^{2-} species, 2D HETCOR NMR revealed contacts between "non-apatitic" PO_4^{3-} ions and water molecules. Hence, in accordance with mineralization studies employing direct HCA precipitation from solution,[8,56–58] the ACP phase initially formed at the MBG surface in SBF comprises H_2O, PO_4^{3-} and HPO_4^{2-} species (besides Ca^{2+} and CO_3^{2-} ions[27]). A minor ordering of ACP was observed after 30 days of MBG-exposure to SBF relative to that after 4 h, as witnessed by slightly better resolved ^{1}H NMR signals from the H_2O and HPO_4^{2-} species.

Whenever primarily focussing is on the ^{1}H environments of the biomimetic phosphate layer, we stress the advantages of using the ^{1}H-detected diffCP-MAS experimental protocol of ref.[17] relative to either a full 2D HETCOR NMR acquisition or time-consuming ^{31}P→^{1}H CPMAS.[14,85,86] Surprisingly, the utility of this technique appears to be overlooked in the community. Besides that ^{1}H–^{31}P diffCP-MAS NMR experimentation offers more rapid NMR acquisitions than single-pulse ^{31}P NMR, we also demonstrated that it is a more sensitive tool for detecting the *onset* of HCA formation, notably so from P-bearing (M)BGs at short SBF-exposure periods, where the ^{31}P resonances of the glass overlap with those from the biomimetic phases, thereby increasing the net peakwidth and obscuring the narrow but very weak NMR signal from HCA.

Acknowledgements

This work was supported by the Swedish Research Council (projects VR-NT 2010-4943 and 2014-4667), and by the Ministerio de Economía y Competitividad, Agencia Estatal de Investigación (AEI) and Fondo Europeo de Desarrollo Regional (FEDER) (projects MAT 2013-43299-R, 2015-64831-R, and 2016-75611-R, AEI/FEDER, UE). M.V.-R. acknowledges funding from the European Research Council (Advanced Grant VERDI; ERC-2015-AdG Proposal 694160). C. T.-I. was supported by a postdoctoral grant from the Carl Trygger Foundation.

References

[1] Weiner, S.; Wagner, H. D. The Material Bone: Structural-Mechanical Function Relations. *Annu. Rep. Mater. Sci.* **1998**, *28*, 271–298.

[2] Olszta, M. J.; Cheng, X.-G.; Jee, S. S.; Kumar, R.; Kim, Y.-Y.; Kaufman, M. J.; Douglas, E. P.; Gower, L. B. Bone Structure and Formation: A New Perspective. *Mater. Sci. Engin.* **2007**, *R58*, 77–116.

[3] Traub, W.; Arad, T.; Weiner, S. Three-Dimensional Ordered Distribution of Crystals in Turkey Tendon Collagen Fibers. *Proc. Nat. Acad. Sci. USA* **1989**, *86*, 9822–9826.

[4] Rey, C.; Combes, C.; Drouet, C.; Glimcher, M. J. Bone Mineral: Update on Chemical Composition and Structure. *Osteoporos. Int.* **2009**, *20*, 1013–1021.

[5] Hu, Y.-Y.; A, Rawal; Schmidt-Rohr, K. Strongly Bound Citrate Stabilizes the Apatite Nanocrystals in Bone. *Proc. Nat. Acad. Sci. USA* **2010**, *107*, 22425–22429.

[6] Wilson, E. E.; Awonsusi, A.; Morris, M. D.; Kohn, D. H.; Tecklenburg, M. M. J.; Beck, L. W. Three Structural Roles of Water in Bone Observed by Solid-State NMR. *Biophys. J.* **2006**, *90*, 3722–3731.

[7] Hu, Y.-Y.; Liu, X. P.; Ma, X.; Rawal, A.; Prozorov, T.; Akinc, M.; Mallapragada, S. K.; Schmidt-Rohr, K. Biomimetic Self-Assembling Copolymer-Hydroxyapatite Nanocomposites with the Nanocrystal Size Controlled by Citrate. *Chem. Mater.* **2011**, *23*, 2481–2490.

[8] Wang, Y.; von Euw, S.; Fernandes, F. M.; Cassaignon, S.; Selmane, M.; Laurant, G.; Pehau-Arnaudet, G.; Coelho, C.; Bonhomme-Coury, L.; Giraud-Guille, M.-M.; et al. Water-Mediated Structuring of Bone Apatite. *Nature Mater.* **2013**, *12*, 1144–1153.

[9] Davies, E.; Müller, K. H.; Wong, W. C.; Pickard, C. J.; Skepper, J. N.; Duer, M. J. Citrate Bridges between Mineral Platelest in Bone. *Proc. Nat. Acad. Sci. USA* **2014**, *111*, E1354–E1363.

[10] Combes, C.; Cazalbou, S.; Rey, C. Apatite Biominerals. *Minerals* **2016**, *6*, 1–25.

[11] Santos, R. A.; Wind, R. A.; Bronnimann, C. E. ^{1}H CRAMPS and ^{1}H-^{31}P HetCor Experiments on Bone, Bone Mineral and Model Calcium Phosphate Phases. *J. Magn. Reson. B* **1994**, *105*, 183–187.

[12] Cho, G.; Wu, Y.; Ackerman, J. L. Detection of Hydroxyl Ions in Bone Mineral by Solid-State NMR Spectroscopy. *Science* **2003**, *300*, 1123–1127.

[13] Kaflak-Hachulska, A.; Samoson, A.; Kolodziejski, W. ^{1}H MAS and ^{1}H $\longrightarrow^{31}$P CP/MAS NMR Study of Human Bone Mineral. *Calcif. Tissue Int.* **2003**, *73*, 476–486.

[14] Kolmas, J.; Kolodziejski, W. Concentration of Hydroxyl Groups in Dental Apatites: A Solid-State ^{1}H MAS NMR Study Using Inverse ^{31}P $\longrightarrow^{1}$H Cross-Polarization. *Chem. Comm.* **2007**, pp. 4390–4392.

[15] Yesinowski, J. P.; Eckert, H. Hydrogen Environments in Calcium Phosphates: ^{1}H MAS NMR at High Spinning Speeds. *J. Am. Chem. Soc.* **1987**, *109*, 6274–6282.

[16] Jäger, C.; Welzel, T.; Meyer-Zaika, W.; Epple, M. A Solid-State NMR Investigation of the Structure of Nanocrystalline Hydroxyapatite. *Magn. Reson. Chem.* **2006**, *44*, 573–580.

[17] Maltsev, S.; Jäger, C. Solid-State NMR Spectroscopy Using the Lost I Spin Magnetization in Polarization Transfer Experiments. *Solid State Nucl. Magn. Reson.* **2008**, *34*, 175–179.

[18] Babonneau, F.; Bonhomme, C.; Hayakawa, S.; Osaka, A. Solid State NMR Characterization of Nano-Crystalline Hydroxy-Carbonate-Apatite Using ^{1}H-^{31}P-^{13}C Triple Resonance Experiments. *Mater. Res. Symp. Proc.* **2007**, *984*.

[19] Mason, H. E.; Kozlowski, A.; Phillips, B. L. Solid-State NMR Study of the Role of H and Na in AB-Type Carbonate Hydroxylapatite. *Chem. Mater.* **2008**, *20*, 294–302.

[20] Nassif, N.; Martineau, F.; Syzgantseva, O.; Gobeaux, F.; Willinger, M.; Coradin, T.; Cassaignon, S.; Azaïs, T.; Giraud-Guille, M. M. *In Vivo* Inspired Conditions to Synthesize Biomimetic Hydroxyapatite. *Chem. Mater.* **2010**, *22*, 3653–3663.

[21] Kolmas, J.; Kolodziejski, W. Incorporation of Carbonate and Magnesium Ions into Synthetic Hydroxyapatite: The Effect on Physiochemical Properties. *J. Mol. Struct.* **2011**, *987*, 40–50.

[22] Ben Osman, M.; Diallo-Garcia, S.; Herledan, V.; Brouri, D.; Yoshioka, T.; Kubo, J.; Millot, Y.; Costentin, G. Discrimination of Surface and Bulk Structure of Crystalline Hydroxyapatite Nanoparticles by NMR. *J. Phys. Chem. C* **2015**, *119*, 23008–23020.

[23] Tseng, Y.-H.; Tsai, Y.-L.; Tsai, T. W. T.; Chao, J. C. H.; Lin, C.-P.; Huang, S.-H.; Mou, Y.; Mou, C.-Y.; Chan, J. C. C. Characterization of the Phosphate Units in Rat Dentin by Solid-State NMR Spectroscopy. *Chem. Mater.* **2007**, *19*, 6088–6094.

[24] Huang, S.-H.; Tsai, Y.-L.; Lee, Y.-L.; Lin, C.-P.; Chan, J. C. C. Structural Model of Rat Dentin Revisited. *Chem. Mater.* **2009**, *21*, 2593–2585.

[25] Roberts, J. E.; Vega, S.; Griffin, R. G. Two-Dimensional Heteronuclear Chemical Shift Correlation Spectroscopy in Rotating Solids. *J. Am. Chem. Soc.* **1984**, *106*, 2506–2512.

[26] Lin, K. S. K.; Tseng, Y.-H.; Mou, Y.; Hsu, Y.-C.; Yang, C.-M.; Chan, J. C. C. Mechanistic Study of Apatite Formation on Bioactive Glass Surface using ^{31}P Solid-State NMR Spectroscopy. *Chem. Mater.* **2005**, *17*, 4493–4501.

[27] Gunawidjaja, P. N.; Lo, A. Y. H.; Izquierdo-Barba, I.; García, A.; Arcos, D.; Stevensson, B.; Grins, J.; Vallet-Regí, M.; Edén, M. Biomimetic Apatite Mineralization Mechanisms of Mesoporous Bioactive Glasses as Probed by Multinuclear ^{31}P, ^{29}Si, ^{23}Na and ^{13}C Solid State NMR. *J. Phys. Chem. C* **2010**, *114*, 19345–19356.

[28] Mathew, R.; Gunawidjaja, P. N.; Izquierdo-Barba, I.; Jansson, K.; García, A.; Arcos, D.; Vallet-Regí, M.; Edén, M. Solid State ^{31}P and ^{1}H NMR Investigations of Amorphous and Crystalline Calcium Phosphates Grown Biomimetically from a Mesoporous Bioactive Glass. *J. Phys. Chem. C* **2011**, *115*, 20572–20582.

[29] Termine, J. D.; Posner, A. S. Infrared Analysis of Rat Bone: Age Dependency of Amorphous and Crystalline Fractions. *Science* **1966**, *153*, 1523–1525.

[30] Blumenthal, N. C.; Posner, A. S. Hydroxyapatite: Mechanism of Formation and Properties. *Calc. Tiss. Res.* **1973**, *13*, 235–243.

[31] Posner, A. S.; Betts, F. Synthetic Amorphous Calcium Phosphate and Its Relation to Bone Mineral Structure. *Acc. Chem. Res.* **1975**, *8*, 273–279.

[32] Klimavicius, V.; Kareiva, A.; Balevicius, V. Solid State NMR Study of Hydroxapatite Containing Amorphous Phosphate Phase and Nanostructured Hydroxapatite: Cut-Off Averaging of CP-MAS Kinetics and Size Profiles of Spin Clusters. *J. Phys. Chem. C* **2014**, *118*, 28914–28921.

[33] Klimavicius, V.; Dagys, L.; Balevicius, V. Subnanoscale Order and Spin Diffusion in Complex Solids Through the Processing of Cross-Polarization Kinetics. *J. Phys. Chem. C* **2016**, *120*, 3542–3549.

[34] Vyalikh, A.; Simon, P.; Kollmann, T.; Kniep, R.; Scheler, U. Local Environment in Biomimetic Hydroxyapatite-Gelatin Nanocomposites as Probed by NMR Spectroscopy. *J. Phys. Chem. C* **2011**, *115*, 1513–1519.

[35] Gunawidjaja, P. N.; Mathew, R.; Lo, A. Y. H.; Izquierdo-Barba, I.; García, A.; Arcos, D.; Vallet-Regí, M.; Edén, M. Local Structures of Mesoporous Bioactive Glasses and their Surface Alterations *In Vitro*: Inferences from Solid State Nuclear Magnetic Resonance. *Phil. Trans. R. Soc. A* **2012**, *370*, 1376–1399.

[36] Souza, M. T.; Crovace, M. C.; Schröder, C.; Eckert, H.; Peitl, O.; Zanotto, E. D. Effect of Magnesium Ion Incorporation on the Thermal Stability, Dissolution Behavior and Bioactivity in Bioglass-Derived Glasses. *J. Non-Cryst. Solids* **2013**, *382*, 57–65.

[37] Hench, L. L. Bioceramics: From Concept to Clinic. *J. Am. Ceram. Soc.* **1991**, *74*, 1487–1510.

[38] Yan, X. X.; Yu, C. Z.; Zhou, X. F.; Tang, J. W.; Zhao, D. Y. Highly Ordered Mesoporous Bioactive Glasses with Superior In Vitro Bone-Forming Bioactivities. *Angew. Chem. Int. Ed.* **2004**, *43*, 5980–5984.

[39] López-Noriega, A.; Arcos, D.; Izquierdo-Barba, I.; Sakamoto, Y.; Terasaki, O.; Vallet-Regí, M. Ordered Mesoporous Bioactive Glasses for Bone Tissue Regeneration. *Chem. Mater.* **2006**, *18*, 3137–3144.

[40] Kim, C. Y.; Clark, A. E.; Hench, L. L. Early Stages of Calcium-Phosphate Layer Formation in Bioglasses. *J. Non-Cryst. Solids* **1989**, *113*, 195–202.

[41] Takadama, H.; Kim, H.-M.; Kokubo, T.; Nakamura, T. Mechanism of Biomineralization of Apatite on a Sodium Silicate Glass: TEM-EDX Study In Vitro. *Chem. Mater.* **2001**, *13*, 1108–1113.

[42] Turdean-Ionescu, C.; Stevensson, B.; Grins, J.; Izquierdo-Barba, I.; García, A.; Arcos, D.; Vallet-Regí, M.; Edén, M. Composition-Dependent *In Vitro* Apatite Formation at Mesoporous Bioactive Glass-Surfaces Quantified by Solid-State NMR and Powder XRD. *RSC Adv.* **2015**, *5*, 86061–86071.

[43] Turdean-Ionescu, C.; Stevensson, B.; Izquierdo-Barba, I.; García, A.; Arcos, D.; Vallet-Regí, M.; Edén, M. Surface Reactions of Mesoporous Bioactive Glasses Monitored by Solid-State NMR: Concentration Effects in Simulated Body Fluid. *J. Phys. Chem. C* **2016**, *120*, 4961–4974.

[44] Leonova, E.; Izquierdo-Barba, I.; Arcos, D.; López-Noriega, A.; Hedin, N.; Vallet-Regí, M.; Edén, M. Multinuclear Solid-State NMR Studies of Ordered Mesoporous Bioactive Glasses. *J. Phys. Chem. C* **2008**, *112*, 5552–5562.

[45] Boskey, A. L. Apatite Biominerals. *J. Cell. Biochem. Suppl.* **1998**, *30-31*, 83–91.

[46] Wu, Y.; Ackerman, J. L.; Strawich, E. S.; Rey, C.; Kim, H.-M.; Glimcher, M. J. Phosphate Ions in Bone: Identification of a Calcium-Organic Phosphate Complex by ^{31}P Solid-State NMR Spectroscopy at Early Stages of Mineralization. *Calcif. Tissue Int.* **2003**, *72*, 610–626.

[47] Nudelman, F.; Pietserse, K.; George, A.; Bomans, P. H. H.; Friedrich, H.; Brylka, L. J.; Hilbers, P. A. J.; de With, G.; Sommerdijk, N. A. J. M. The Role of Collagen in Bone Apatite Formation in the Presence of Hydroxyapatite Nucleation Inhibitors. *Nature Mater.* **2010**, *9*, 1004–1009.

[48] Wang, Y.; Azaïs, T.; Robin, M.; Vallée, A.; Catania, C.; Legriel, P.; Pehau-Arnaudet, G.; Babonneau, F.; Giraud-Guille, M.-M.; Nassif, N. The Predominant Role of Collagen in the Nucleation, Growth, Structure and Orientation of Bone Apatite. *Nature Mater.* **2012**, *11*, 724–733.

[49] Weiner, S. Transient Precursor Strategy or Very Small Biological Apatite Crystals? *Bone* **2006**, *39*, 431–433.

[50] Grynpas, M. D.; Omelon, S. Transient Precursor Strategy or Very Small Biological Apatite Crystals?. *Bone* **2007**, *41*, 162–164.

[51] Celotti, G.; Tampieri, A.; Spirio, S.; Landi, E.; Bertinetti, L.; Martra, G.; Ducati, C. Crystallinity in Apatites: How Can a Truly Disordered Fraction be Distinguished from Nanosize Crystalline Domains?. *J. Mater. Sci: Mater. Med.* **2006**, *17*, 1079–1087.

[52] Brown, W. E.; Lehr, J. R.; Smith, J. P.; Frazier, A. W. Crystallography of Octacalcium Phosphate. *J. Am. Chem. Soc.* **1957**, *79*, 5318–5319.

[53] Brown, W. E.; Eidelman, N.; Tomazic, B. Octacalcium Phosphate as a Precursor in Biomineral Formation. *Adv. Dental Res.* **1987**, *1*, 306–313.

[54] Christoffersen, J.; Christoffersen, M. R.; Kibalczyc, W.; Andersen, F. A. A contribution to the Understanding of the Formation of Calcium Phosphates. *J. Cryst. Growth* **1989**, *94*, 767–777.

[55] Wang, C.-G.; J.-W. Liao, B.-D. Gou; Huang, J.; Tang, R.-K.; Tao, J.-H.; Zhang, T.-L.; Wang, K. Crystallization at Multiple Sites Inside Particles of Amorphous Calcium Phosphate. *Cryst. Growth Design* **2009**, *9*, 2620–2626.

[56] Habraken, W. J. E. M.; Tao, J.; Brylka, L. J.; Friedrich, H.; Bertinetti, L.; Schenk, A. S.; Verch, A.; Dmitrovich, V.; Bomans, P. H. H.; Frederik, P. M.; et al., Ion-Association Complexes Unite

Classical and Non-Classical Theories for the Biomimetic Nucleation of Calcium Phosphate. *Nature Commun.* **2013**, *4*, 1507:1–12.

[57] Xie, B.; Halter, T. J.; Borah, B. M.; Nancollas, G. H. Tracking Amorphous Precursor Formation and Transformation During Induction States of Nucleation. *Cryst. Growth Design* **2014**, *14*, 1659–1665.

[58] Ibsen, C. J. S.; Chernyshov, D.; Birkedal, H. Apatite Formation from Amorphous Calcium Phosphate and Mixed Amorphous Calcium Phosphate/Amorphous Calcium Carbonate. *Chem. Eur. J.* **2016**, *22*, 12347–12357.

[59] Chen, W.-Y.; Yang, C.-I.; Lin, C.-J.; Huang, S.-J.; Chan, J. C. C. Characterization of the Crystallization Pathway Calcium Phosphate in Liposomes. *J. Phys. Chem. C* **2014**, *118*, 12022–12027.

[60] Gunawidjaja, P. N.; Izquierdo-Barba, I.; Mathew, R.; Jansson, K.; García, A.; Grins, J.; Arcos, D.; Vallet-Regí, M.; Edén, M. Quantifying Apatite Formation and Cation Leaching from Mesoporous Bioactive Glasses *In Vitro*: a SEM, Solid-State NMR and Powder XRD Study. *J. Mater. Chem.* **2012**, *22*, 7214–7223.

[61] Crane, N. J.; Popescu, V.; Morris, M. D.; Steenhuis, P.; Ignelzi Jr, M. A. Raman Spectroscopic Evidence for Octacalcium Phosphate and Other Transient Mineral Species Deposited During Intramembraneous Mineralization. *Bone* **2006**, *39*, 434–442.

[62] Beniash, E.; Metzler, R. A.; Lam, R. S. K.; Gilbert, P. U. P. A. Transient Amorphous Calcium Phosphate in Forming Enamel. *J. Struct. Biol.* **2009**, *166*, 133–143.

[63] Mahamid, J.; Aichmayer, B.; Shimoni, E.; Ziblat, R.; Li, C.; Siegel, S.; Paris, O.; Fratzl, P.; Weiner, S.; Addadi, L. Mapping Amorphous Calcium Phosphate Transformation into Crys-

talline Mineral from the Cell to the Bone in Zebrafish Fin Rays. *Proc. Nat. Acad. Sci. USA* **2010**, *107*, 6316–6321.

[64] Akiva, A.; Kerschnitzki, M.; Pinkas, I.; Wagemaier, W.; Yaniv, K.; Fratzl, P.; Addadi, L.; Weiner, S. Mineral Formation in the Larval Zebrafish Tail Bone Occurs via an Acidic Disordered Calcium Phosphate Phase. *J. Am. Chem. Soc.* **2016**, *138*, 14481–14487.

[65] Eichert, D.; Sfihi, H.; Combes, C.; Rey, C. Specific Characterisitics of Wet Nanocrystalline Apatites: Consequences on Biomaterials and Bone Tissue. *Key. Eng. Mater.* **2004**, *254-256*, 927–930.

[66] Wu, Y.; Ackerman, J. L.; Kim, H.-M.; Rey, C.; Barrough, A.; Glimcher, M. J. Nuclear Magnetic Resonance Spin-Spin Relaxation of the Crystals of Bone, Dental Enamel, and Synthetic Hydroxyapatites. *J. Bone Miner. Res.* **2002**, *17*, 472–480.

[67] Cazalbou, S.; Combes, C.; Eichert, D.; Rey, C.; Glimcher, M. J. Poorly Crystalline Apatites: Evolution and Maturation In Vitro and In Vivo. *J. Bone Miner. Metab.* **2004**, *22*, 310–317.

[68] Brinker, C. J.; Lu, Y.; Sellinger, A.; Fan, H. Evaporation-Induced Self-Assembly: Nanostructures Made Easy. *Adv. Mater.* **1999**, *11*, 579–585.

[69] García, A.; Cicuéndez, M.; Izquierdo-Barba, I.; Arcos, D.; Vallet-Regí, M. Essential Role of Calcium Phosphate Heterogeneities in 2D-Hexagonal and 3D-Cubic SiO_2–CaO–P_2O_5 Mesoporous Bioactive Glasses. *Chem. Mater.* **2009**, *21*, 5474–5484.

[70] Kokubo, T.; Kushitani, H.; Sakka, S.; Kitsugi, T.; Yamamuro, T. Solutions Able to Reproduce *In Vivo* Surface-Structure Changes in Bioactive Glass-Ceramic A-W[3]. *J. Biomed. Mater. Res.* **1990**, *24*, 721–734.

[71] Lo, A. Y. H.; Edén, M. Efficient Symmetry-Based Homonuclear Dipolar Recoupling of Quadrupolar Spins: Double-Quantum NMR Correlations in Amorphous Solids. *Phys. Chem. Chem. Phys.* **2008**, *10*, 6635–6644.

[72] Teymoori, G.; Pahari, B.; Stevensson, B.; Edén, M. Low-Power Broadband Homonuclear Dipolar Recoupling Without Decoupling: Double-Quantum ^{13}C NMR Correlations at Very Fast Magic-Angle Spinning. *Chem. Phys. Lett.* **2012**, *547*, 103–109.

[73] Teymoori, G.; Pahari, B.; Edén, M. Low-Power Broadband Homonuclear Dipolar Recoupling in MAS NMR by Two-Fold Symmetry Pulse Schemes for Magnetization Transfers and Double-Quantum Excitation. *J. Magn. Reson.* **2015**, *261*, 205–220.

[74] States, D. J.; Haberkorn, R. A.; Ruben, D. J. A Two-Dimensional Nuclear Overhauser Experiment with Pure Absorption Phase in Four Quadrants. *J. Magn. Reson.* **1982**, *48*, 286–292.

[75] Mathew, R.; Turdean-Ionescu, C.; Stevensson, B.; Izquierdo-Barba, I.; García, A.; Arcos, D.; Vallet-Regí, M.; Edén, M. Direct Probing of the Phosphate-Ion Distribution in Bioactive Silicate Glasses by Solid-State NMR: Evidence for Transitions between Random/Clustered Scenarios. *Chem. Mater.* **2013**, *25*, 1877–1885.

[76] Stevensson, B.; Mathew, R.; Edén, M. Assessing the Phosphate Distribution in Bioactive Phosphosilicate Glasses by ^{31}P Solid-State NMR and MD Simulations. *J. Phys. Chem. B* **2014**, *118*, 8863–8876.

[77] Berglund, B.; Vaughan, R. W. Correlations Between Proton Chemical Shift Tensors, Deuterium Quadrupole Couplings, and Bond Distances in Solids. *J. Chem. Phys.* **1980**, *73*, 2037–2043.

[78] Brunner, E.; Sternberg, U. Solid-State NMR Investigatios on the Nature of Hydrogen Bonds. *Prog. NMR Spectrosc.* **1998**, *32*, 21–57.

[79] Bronnimann, C. E.; Ziegler, R. C.; Maciel, G. E. Proton NMR Study of Dehydration of the Silica Gel Surface. *J. Am. Chem. Soc.* **1988**, *110*, 2023–2026.

[80] Liu, C. C.; Maciel, G. E. The Fumed Silica Surface: A Study by NMR. *J. Am. Chem. Soc.* **1996**, *118*, 5103–5119.

[81] Grünberg, B.; Emmler, T.; Gedat, E.; Shenderovich, I.; Findenegg, G. H.; Limbach, H.-H.; Buntkowsky, G. Hydrogen Bonding of Water Confined in Mesoporous Silica MCM-41 and SBA-15 Studied by ^{1}H Solid-State NMR. *Chem. Eur. J.* **2004**, *10*, 5689–5696.

[82] Trébosc, J.; Wiench, J. W.; Huh, S.; Lin, V. S.-Y.; Pruski, M. Solid-State NMR Study of MCM-41-Type Mesoporous Silica Nanoparticles. *J. Am. Chem. Soc.* **2005**, *127*, 3057–3068.

[83] Kohn, S. C.; Dupree, R.; Smith, M. E. Proton Environments and Hydrogen-Bonding in Hydrous Silicate Glasses from Proton NMR. *Nature* **1989**, *337*, 539–541.

[84] Robert, E.; Whittington, A.; Fayon, F.; Pichavant, M.; Massiot, D. Structural Characterization of Water-Bearing Silicate and Aliminosilicate Glasses by High-Resolution Solid-State NMR. *Chem. Geol.* **2001**, *174*, 291–305.

[85] Crosby, R. C.; Reese, R. L.; Haw, J. F. Cross Polarization Magic Angle Spinnning Proton NMR Spectroscopy of Solids. *J. Am. Chem. Soc.* **1988**, *110*, 8550–8551.

[86] Isobe, T.; Nakamura, S.; Nemoto, R.; Senna, M. Solid-State Double Nuclear Magetic Resonance Study of the Local Structure of Calcium Phosphate Nanoparticles Synthesized by a Wet-Mechanochemical Reaction. *J. Phys. Chem. B* **2002**, *106*, 5169–5176.

[87] Sandström, D. E.; Jarlbring, M.; Antzutkin, O. N.; Forsling, W. A Spectroscopic Study of Calcium Surface Sites and Adsorbed Iron Species at Aqueous Flouorapatite by Means of ^{1}H and ^{31}P MAS NMR. *Langmuir* **2006**, *22*, 11060–11064.

[88] Dietrich, E.; Oudadesse, H.; Le Floch, M.; Bureau, B.; Gloriant, T. In Vitro Chemical Reactivity of Doped Bioactive Glasses: An Original Approach by Solid-State NMR Spectroscopy. *Adv. Engin. Mater.* **2009**, *11*, B98–B105.

[89] Brunauer, S.; Emmett, P. H.; Teller, E. Adsorption of Gases in Multimolecular Layers. *J. Am. Chem. Soc.* **1938**, *60*, 309–319.

[90] Gregg, S. J.; Sing, K. S. W., *Adsorption, Surface Area, and Porosity*, Academic Press London, New York **1982**,.

[91] Barrett, E. P.; Joyner, L. G.; Halenda, P. P. The Determination of Pore Volume and Area Distributions in Porous Substances. I. Computations from Nitrogen Isotherms. *J. Am. Chem. Soc.* **1951**, *73*, 373–380.

Table 1: MBG Compositions and Textural Properties[a]

Sample	aCaO	$b$$SiO_2$	$c$$P_2O_5$	Stoichiometric Formula[b]	S_{BET} (m^2g^{-1})[c]	V_p (cm^3g^{-1})[d]	d_p (nm)[e]	Mesoporous structure
S90	10.0(9.6)	90.0(90.4)	0.0(0.0)	$Ca_{9.6}Si_{90.4}P_{0.0}O_{190.4}$	468	0.63	5.37	$p6mm$
S85	10.0(10.6)	85.0(86.5)	5.0(2.9)	$Ca_{10.3}Si_{84.1}P_{5.6}O_{192.5}$	480	0.64	5.38	$Ia\bar{3}d$
S58	37.0(36.6)	58.0(59.0)	5.0(4.4)	$Ca_{35.1}Si_{56.5}P_{8.4}O_{169.2}$	195	0.46	9.45	$p6mm$

[a]Each MBG sample is denoted Sb, where b is the *nominal* oxide equivalent of SiO_2 in mol% of the composition aCaO–$b$$SiO_2$–$c$$P_2O_5$, where a+b+c=100 mol%. Values in parentheses represent the experimentally *analyzed* oxide equivalents (see ref.[42]). [b]Charge-balanced analyzed stoichiometric composition, with cation coefficients summing to 100.0 (mol). [c]Specific surface area determined by the Brunauer-Emmett-Teller method.[89] [d]Total pore volume calculated from the amount of N_2 adsorbed at a relative pressure of P/P_0=0.98 according to Gregg *et al.*[90] [e]Average pore diameter obtained by the Barrett-Joyner-Halenda procedure.[91] All data are reproduced from Turdean-Ionescu *et al.*[42]

Figure Captions

Fig. 1. ^{1}H MAS NMR spectra recorded by single pulses (B_0 = 9.4 T; ν_r = 7.00 kHz) from the series of S90-τ_{SBF} (left panel), S85-τ_{SBF} (mid panel), and S58-τ_{SBF} (right panel) MBG specimens, with the SBF-exposure period (τ_{SBF}) increasing from top to bottom. The results for MBG-1d are representative also for those of MBG-4h and MBG-8h (not shown). The spectra are zoomed around the main centerband signals, and are normalized to equal areas across this spectral region. Asterisks mark narrow resonances around {3.6, 1.3, 1.1, 0.8} ppm that stem from OC$\mathbf{H}_2$ and C$\mathbf{H}_3$ moieties of remnant templating molecules, whereas "#" identifies the NMR peak associated with SiO$\mathbf{H}_{\mathrm{isol}}$ groups (only visible from the pristine MBGs). The grey boxes convey the *approximate* shift-ranges representative for SiO**H** moieties experiencing weak, moderate, and strong H-bonding (in practice, their shift-spans overlap are not accurately known).

Fig. 2. (a) 2Q–1Q correlation ^{1}H NMR spectrum recorded from the pristine S90 MBG (B_0 =14.1 T; ν_r =66.00 kHz), using the $[S\mathrm{R}2^{1}_{4}]$ dipolar recoupling sequence with a 242 μs 2QC excitation period. The 2D NMR spectrum is shown together with projections along the horizontal 1Q (top) and vertical 2Q (right) dimension. The topmost 1D NMR spectrum ("1pls") was recorded directly by single pulses under otherwise identical conditions, and processed using the same apodization (60 Hz Lorentzian shape) as that for the 2Q–1Q NMR spectrum. The grey box marks the approximate resonance-region associated with weakly H-bonded SiOH groups, asterisks indicate signals from organic molecules, and "#" identifies the NMR peak from $\mathrm{SiOH}_{\mathrm{isol}}$ moieties. (b) Slices extracted at the as-indicated 2Q shifts ($\delta_{2\mathrm{Q}}$).

Fig. 3. (a) 2Q–1Q correlation ^{1}H NMR spectrum acquired from the S58-15d sample at B_0 =14.1 T and ν_r =66.00 kHz. (b) Slices extracted at the as-indicated 2Q shifts ($\delta_{2\mathrm{Q}}$). See the Caption of Fig. **2** for further information.

Fig. 4. ^{1}H–^{31}P HETCOR 2D NMR spectrum (left panel) recorded from S85-1d at B_0 = 9.4

T and ν_r = 10.00 kHz (τ_{CP} = 1.0 ms), and shown together with its projections along the ^{31}P (horizontal; top) and ^{1}H (vertical; right) spectral dimensions. The right panel displays slices along the ^{31}P dimension, corresponding to $\mathbf{P}O_4^{3-}$/O**H** correlations of HCA (δ_H = 0.0 ppm), as well as non-apatitic $\mathbf{P}O_4^{3-}$/$\mathbf{H}_2$O (δ_H = 5.8 ppm) and $\mathbf{HP}O_4^{2-}$ (δ_H = 12.1 ppm) contacts of ACP. The ^{31}P fwhm values are given at the right spectral portions of the slices. The lowest 2D contour level is at 6% of the maximum amplitude.

Fig. 5. ^{1}H NMR spectra of the indicated MBG-4h (top panel) or MBG-30d specimens (bottom panel); they were recorded either directly by single pulses ("1pls") or by the ^{1}H–^{31}P "diffCP" protocol,[17] the latter labeled by the respective contact interval (τ_{CP}) of 0.2 ms or 6.0 ms used for ^{1}H→^{31}P CPMAS. The NMR spectra are normalized to equal areas. The broad resonances, emphasized in the NMR spectra obtained with τ_{CP} = 0.2 ms and peaking ≈5 ppm and ≈12 ppm stem from $\mathbf{H}_2$O and $\mathbf{H}PO_4^{2-}$ moieties, respectively. The weak but sharp peak at 10 ppm (marked by an asterisk) is attributed to the $\mathbf{H}PO_4^{2-}$ group of brushite.[11–13,15]

Fig. 6. ^{1}H NMR spectra recorded at 9.4 T and 14.00 kHz MAS from two distinct HA powders, labelled (a) HA–1 and (b) HA–2; they are associated with "low" and moderately "high" surface hydration degrees, respectively, as witnessed by the broad NMR peak centered at 5.5 ppm from HA–2. Both samples manifest the HA-characteristic O**H** resonance ≈ 0 ppm. (c) The result after soaking the HA–2 powder in ethanol (red trace), as well as after repacking the powder and repeating the NMR experiment (black trace).

Fig. 7. Schematic illustrations of apatite crystallization from ACP, highlighting the equivalence between the disordered surface layer of H(C)A[4,8,10,16,65,66] and ACP. (a) Cross-section of a "HA particle" composed of a crystalline apatite core (red) and an amorphous surface layer rich in water and non-apatitic PO_4^{3-} and HPO_4^{2-} species (blue). (b) A distribution of such particles with variable core and shell volumes, where the "innermost" crystallites feature thinner surface layers, while the

ACP-like layer is emphasized in the "outer" parts of the particle ensemble. (c) A few HA crystallites in a dominating matrix of spherical ACP particles (blue); here it appears most natural to consider the system as comprised by two separate HA and ACP phases. (d) HA particles, each coated by a surface layer, which represents the remaining of the ACP phase in (c); the domination of well-crystalline material renders the core-shell interpretation [see (a, b)] most appropriate.

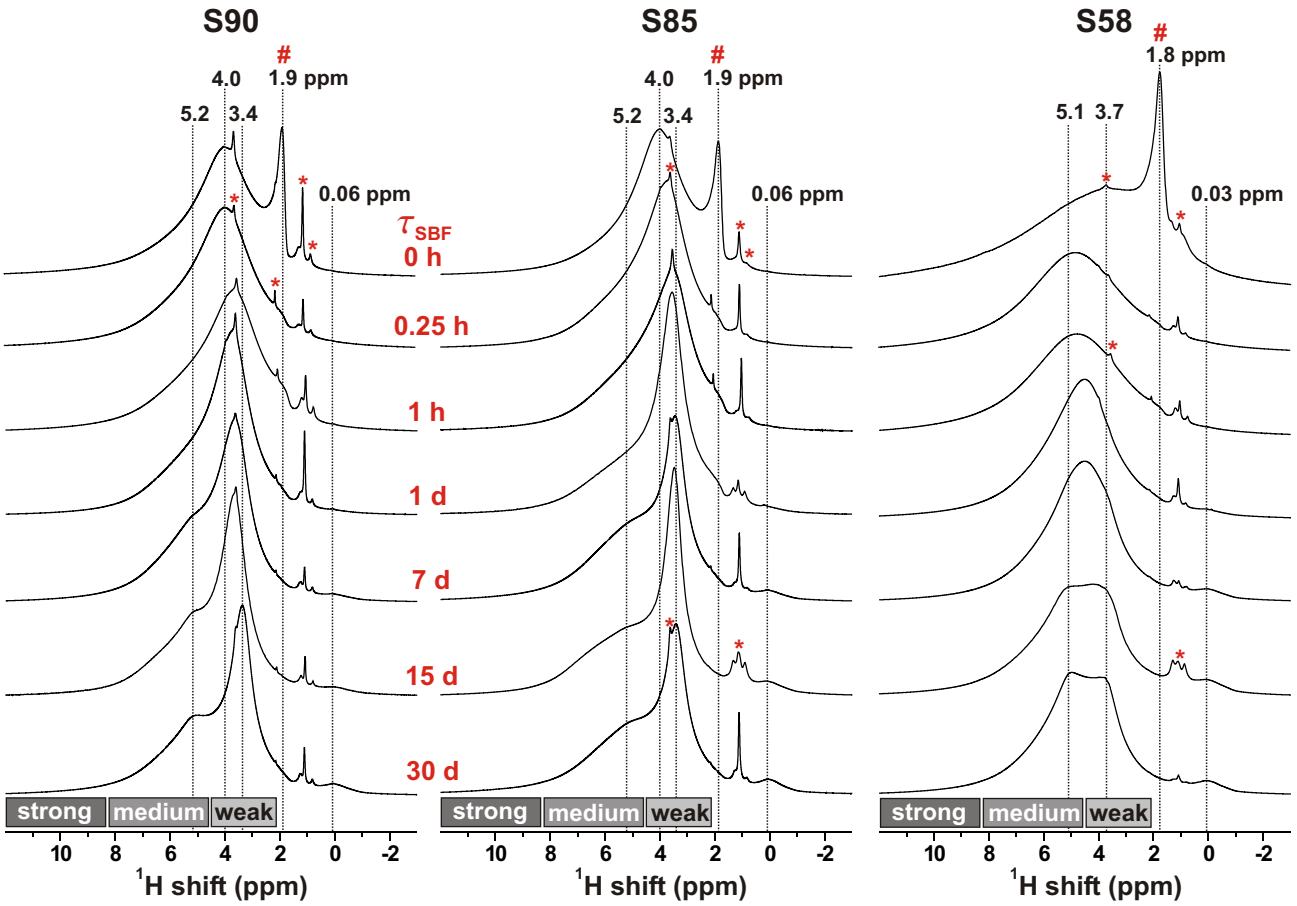
S90
S85
S58
#
1.9 ppm
1.8 ppm
4.0
5.2
3.4
5.1
3.7
0.06 ppm
0.03 ppm
*
τSBF
0 h
0.25 h
1 h
1 d
7 d
15 d
30 d
strong
medium
weak
10
8
6
4
2
0
-2
1H shift (ppm)

Fig. 1

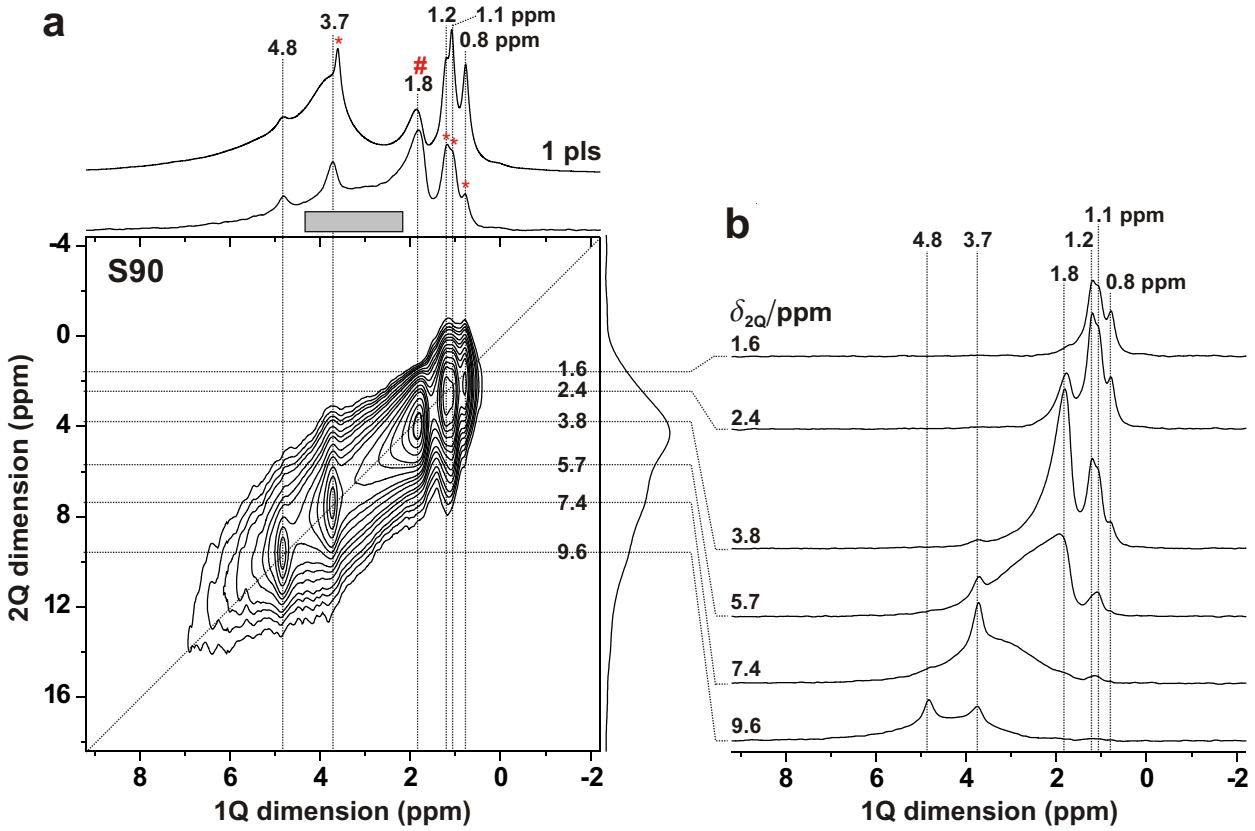
a
4.8
3.7
1.2
1.1 ppm
0.8 ppm
1.8
1 pls
S90
2Q dimension (ppm)
1Q dimension (ppm)
1.6
2.4
3.8
5.7
7.4
9.6
b
δ_{2Q}/ppm

Fig. 2

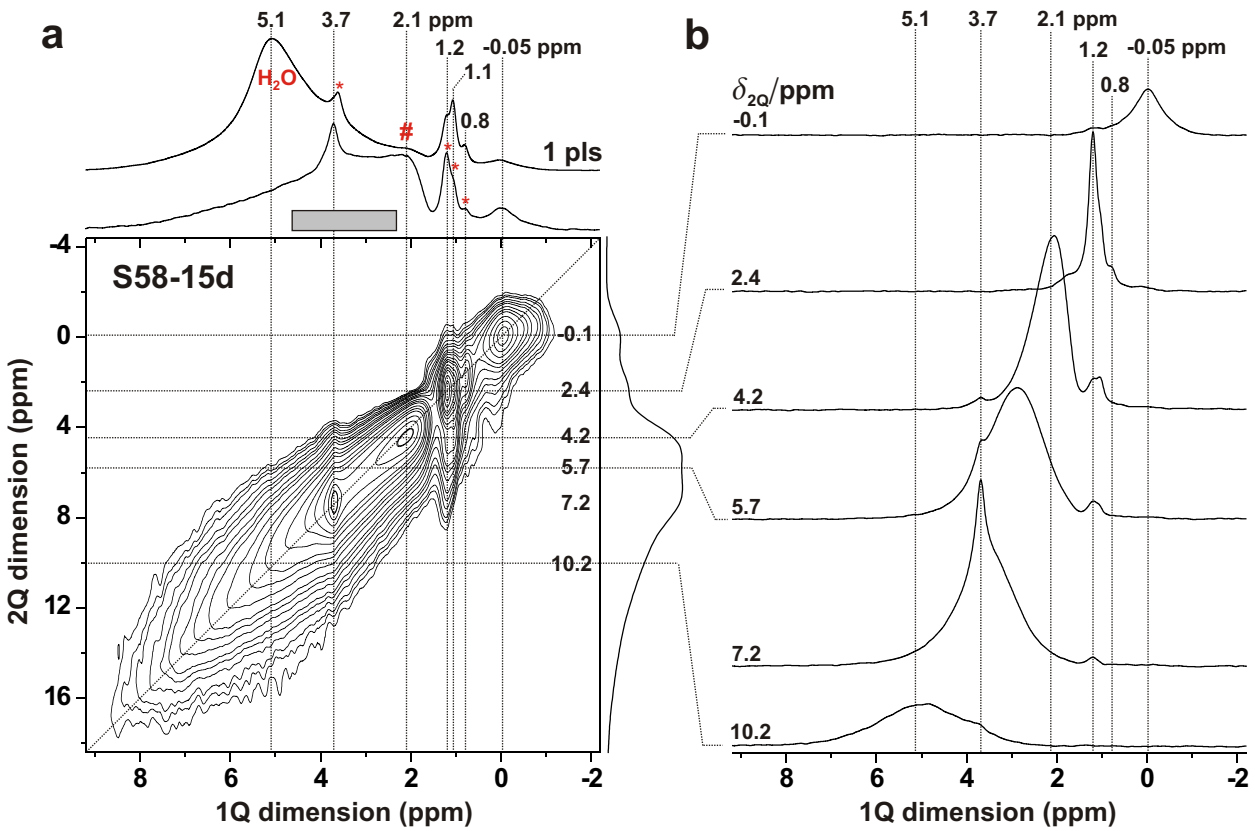
a
5.1
3.7
2.1 ppm
1.2
-0.05 ppm
1.1
0.8
H2O
#
1 pls
S58-15d
2Q dimension (ppm)
1Q dimension (ppm)
-0.1
2.4
4.2
5.7
7.2
10.2
b
δ2Q/ppm

Fig. 3

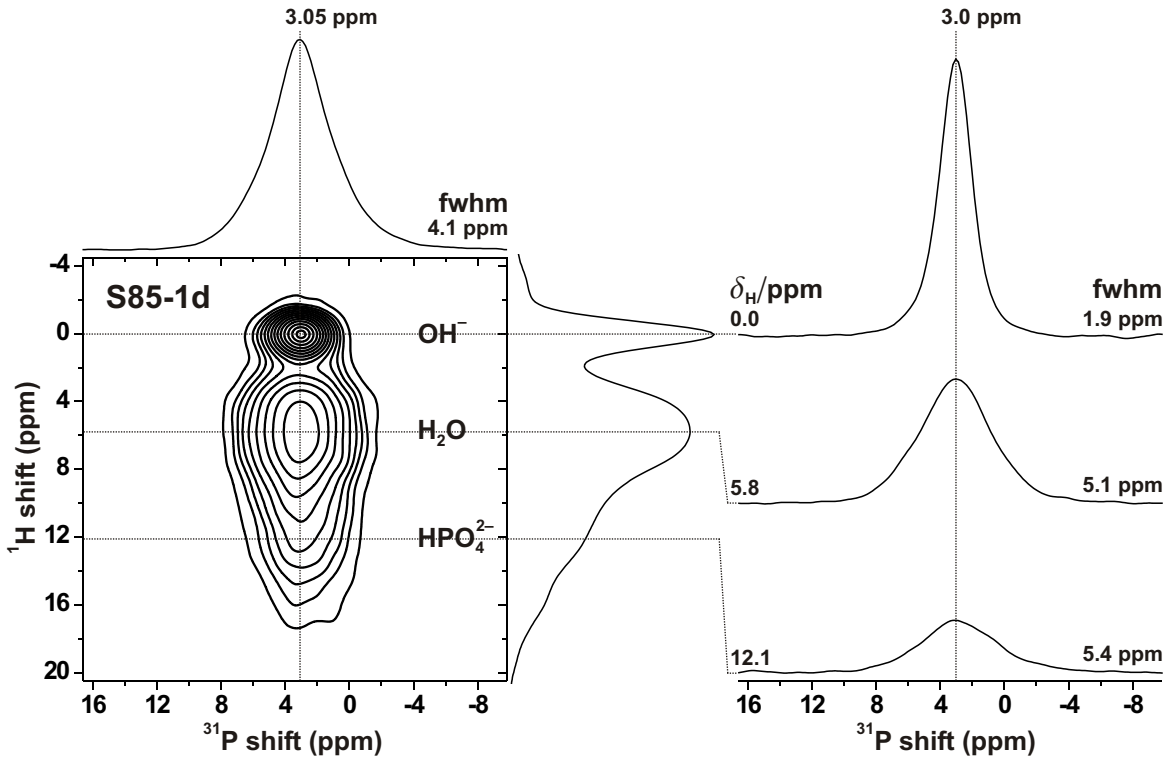
3.05 ppm
fwhm
4.1 ppm
S85-1d
OH⁻
H2O
HPO4 2−
1H shift (ppm)
31P shift (ppm)
δH/ppm
0.0
3.0 ppm
fwhm
1.9 ppm
5.8
5.1 ppm
12.1
5.4 ppm
31P shift (ppm)

Fig. 4

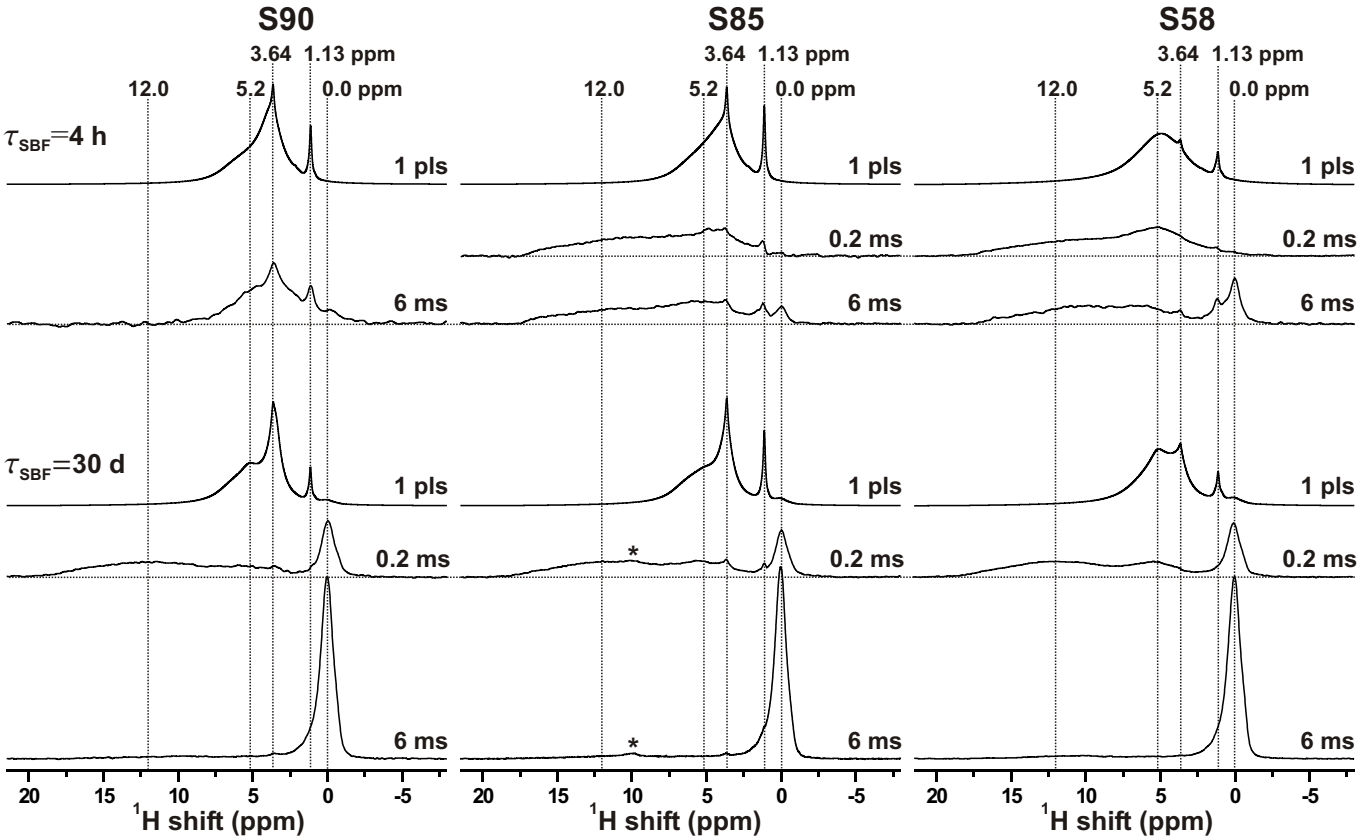
S90
S85
S58
3.64 1.13 ppm
12.0
5.2
0.0 ppm
τSBF=4 h
τSBF=30 d
1 pls
0.2 ms
6 ms
*
20 15 10 5 0 -5
1H shift (ppm)

Fig. 5

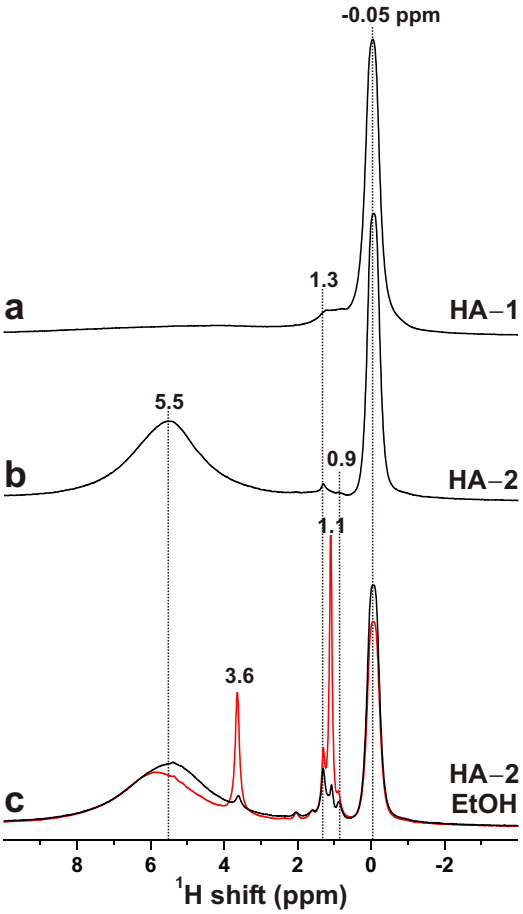

Fig. 6

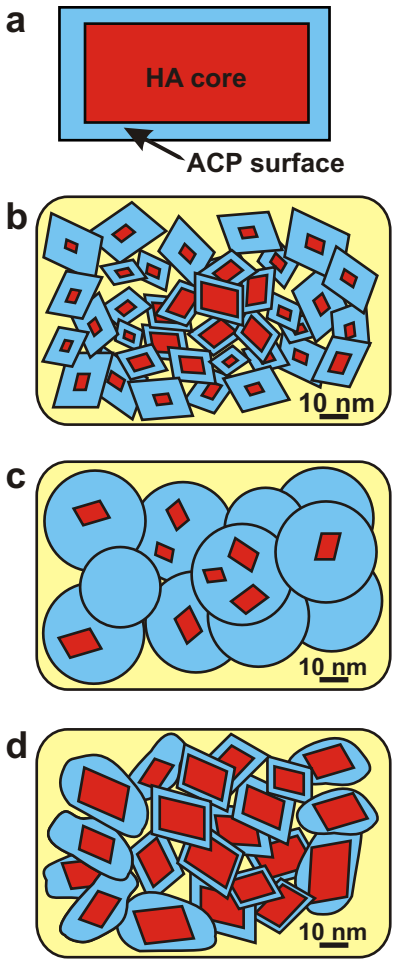

Fig. 7

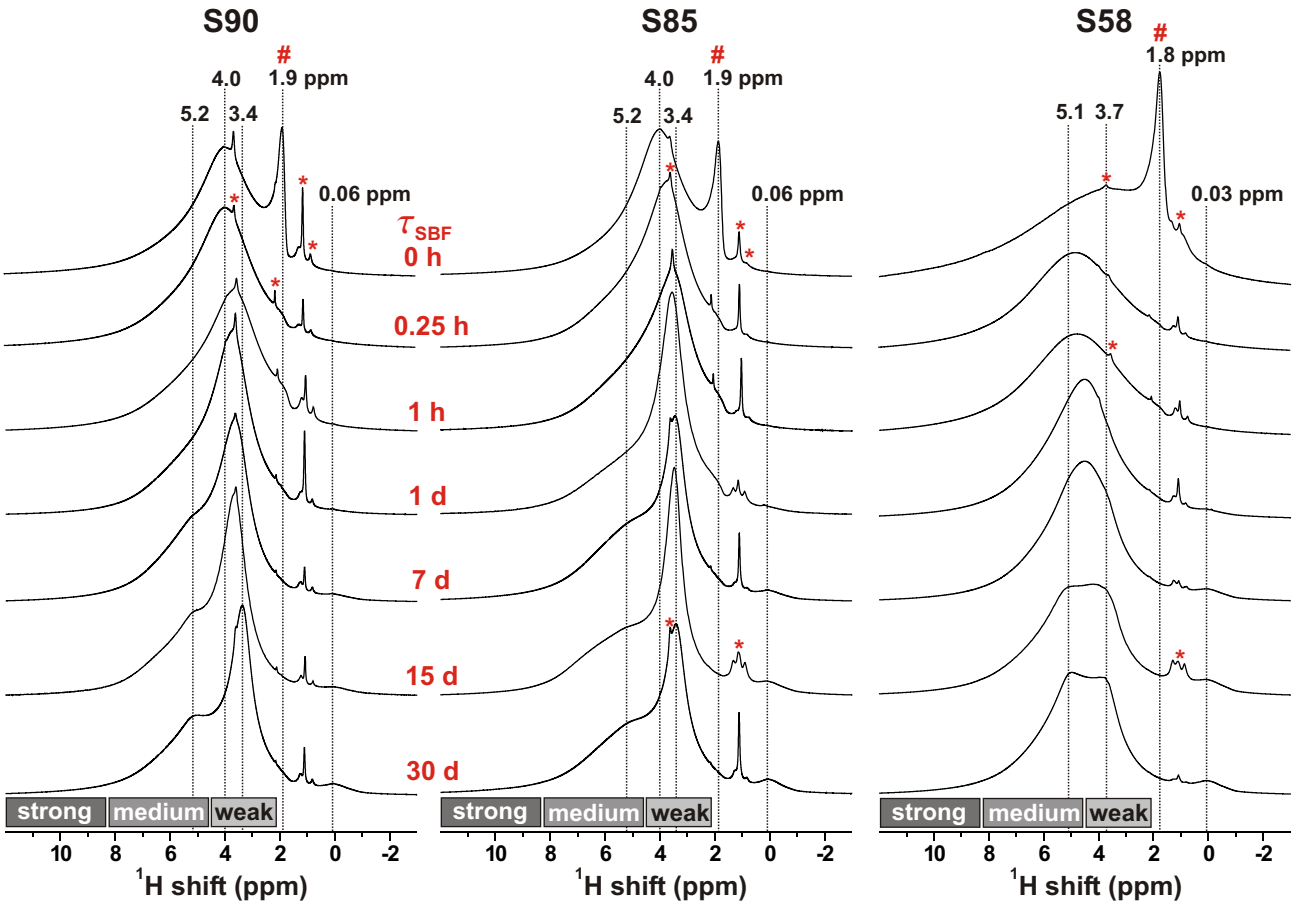
S90
S85
S58
#
1.9 ppm
1.8 ppm
4.0
5.2
3.4
5.1
3.7
0.06 ppm
0.03 ppm
*
τSBF
0 h
0.25 h
1 h
1 d
7 d
15 d
30 d
strong
medium
weak
10 8 6 4 2 0 -2
1H shift (ppm)

Fig. 1

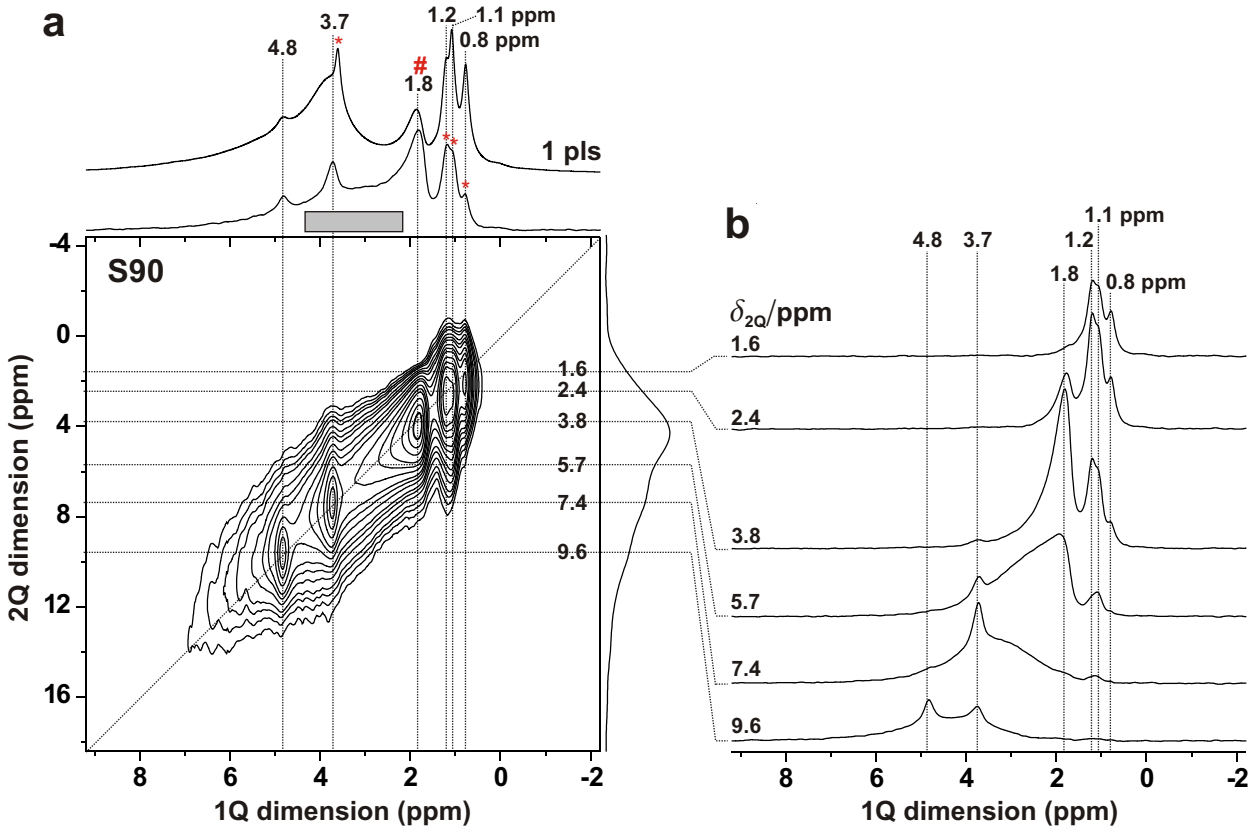
a
4.8
3.7
1.2
1.1 ppm
0.8 ppm
#
1.8
1 pls
S90
2Q dimension (ppm)
1Q dimension (ppm)
1.6
2.4
3.8
5.7
7.4
9.6
b
δ_{2Q}/ppm

Fig. 2

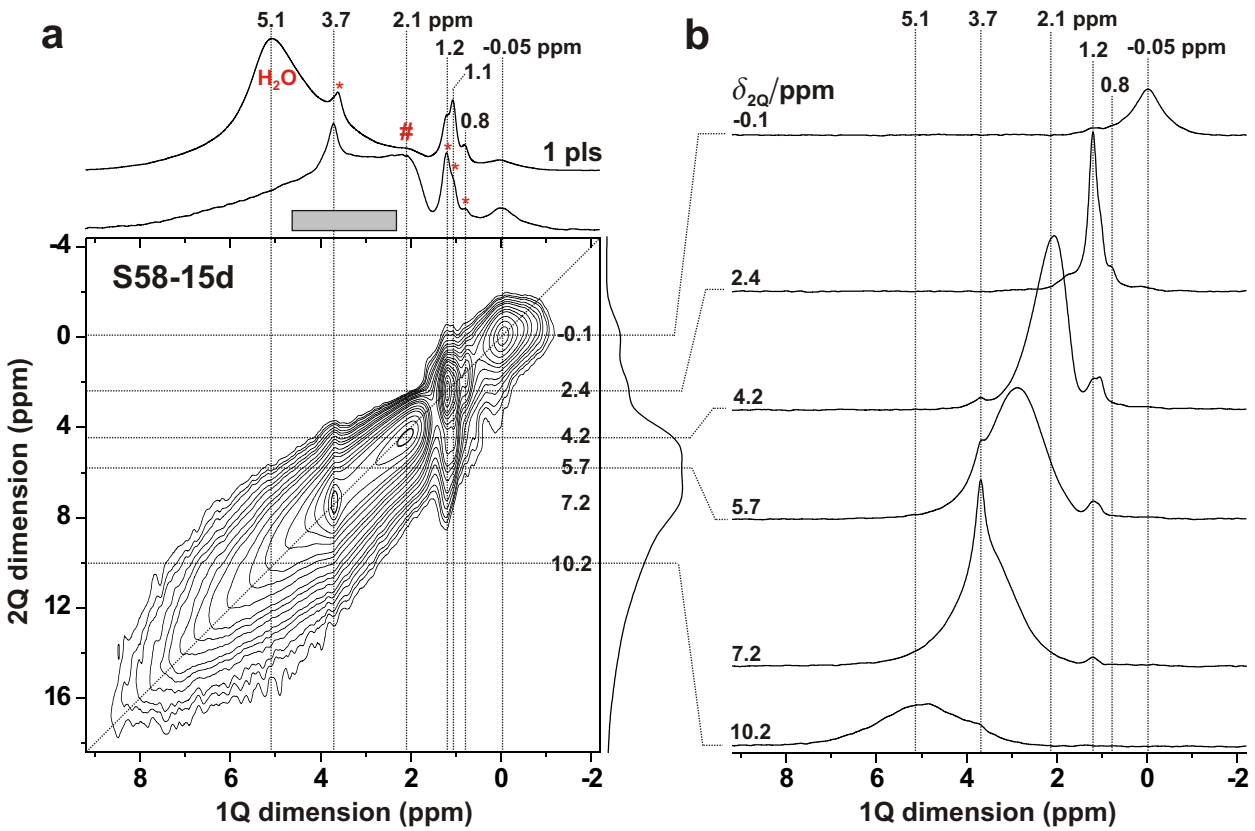
a
5.1
3.7
2.1 ppm
1.2
-0.05 ppm
1.1
0.8
H2O
*
#
1 pls
S58-15d
2Q dimension (ppm)
1Q dimension (ppm)
-0.1
2.4
4.2
5.7
7.2
10.2
b
δ2Q/ppm

Fig. 3

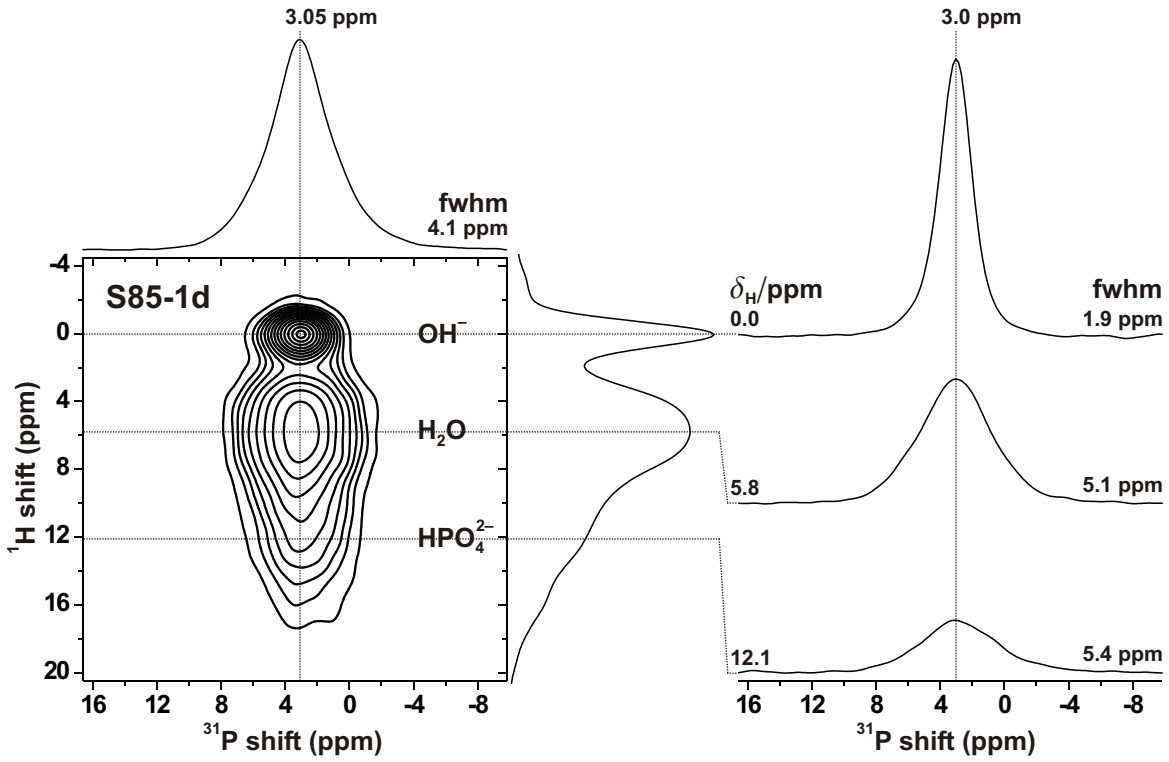
3.05 ppm
fwhm
4.1 ppm
S85-1d
OH⁻
H2O
HPO4 2−
1H shift (ppm)
31P shift (ppm)
δH/ppm
0.0
3.0 ppm
fwhm
1.9 ppm
5.8
5.1 ppm
12.1
5.4 ppm
31P shift (ppm)

Fig. 4

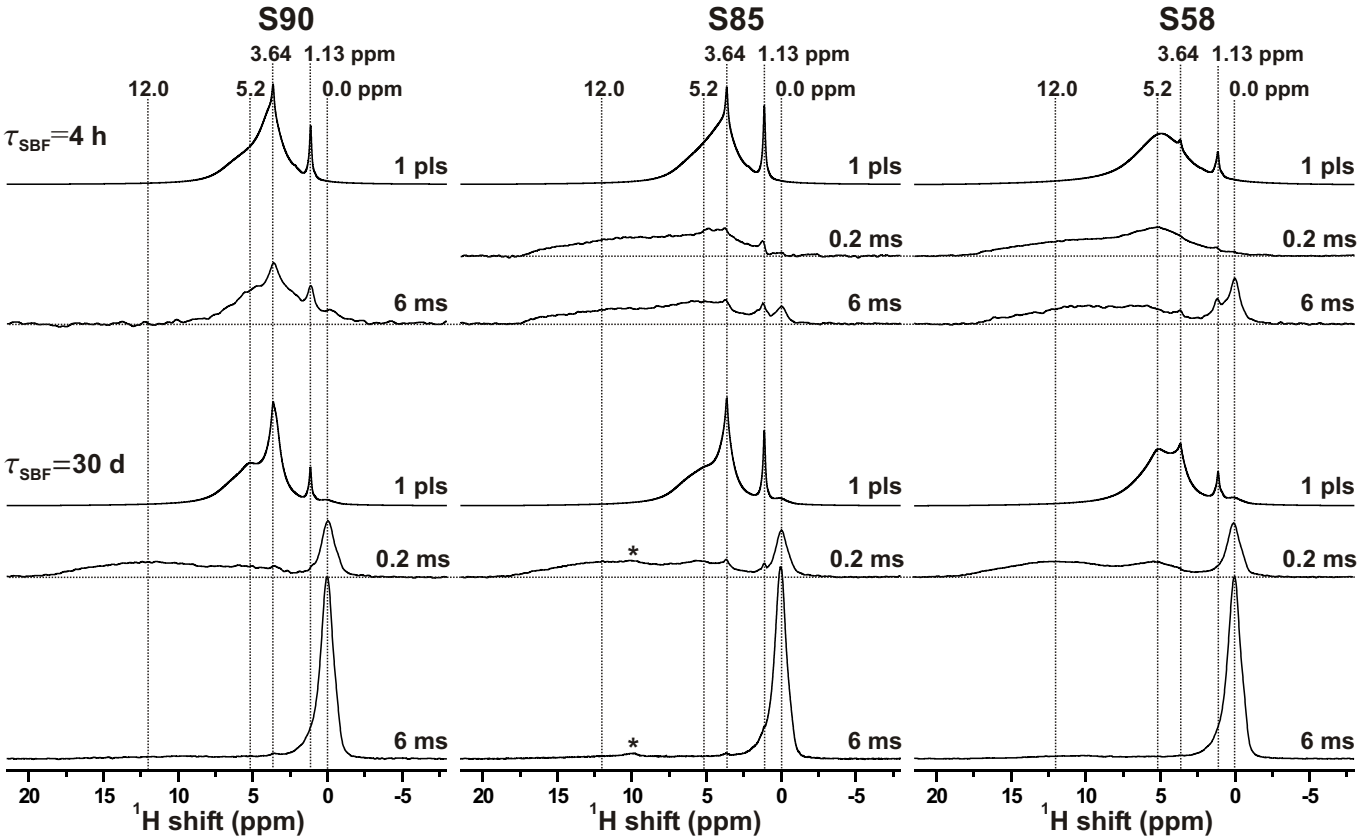
S90
S85
S58
3.64 1.13 ppm
12.0
5.2
0.0 ppm
τSBF=4 h
τSBF=30 d
1 pls
0.2 ms
6 ms
*
20 15 10 5 0 -5
1H shift (ppm)

Fig. 5

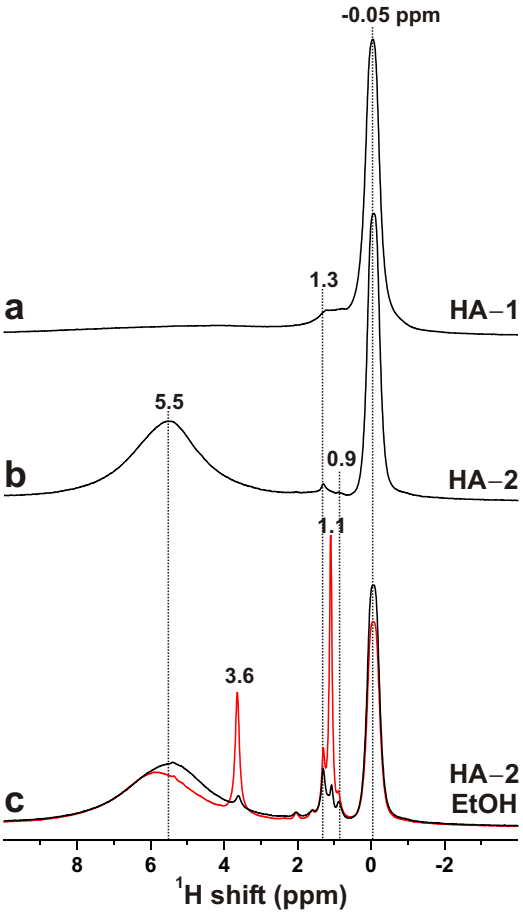

Fig. 6

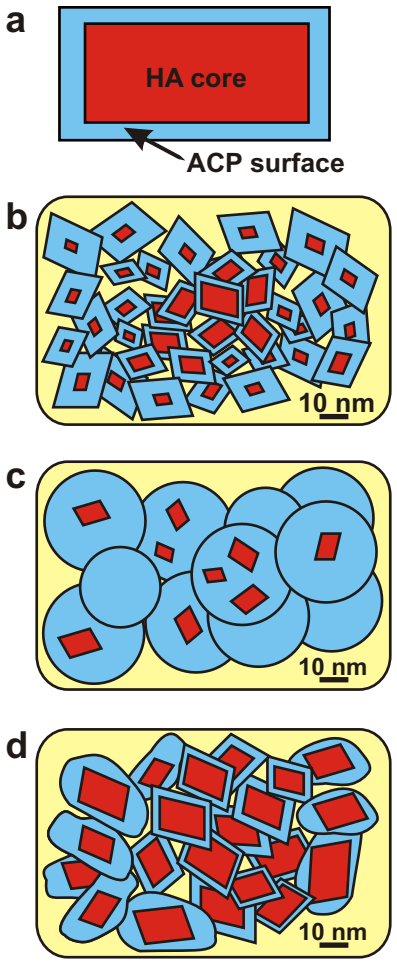

Fig. 7

TOC-Graphic

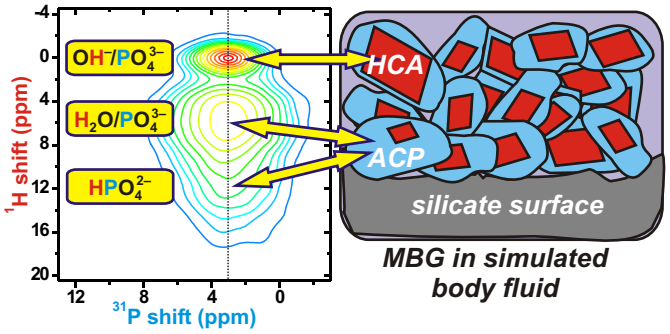
OH⁻/PO4 3−
H2O/PO4 3−
HPO4 2−
1H shift (ppm)
31P shift (ppm)
HCA
ACP
silicate surface
MBG in simulated body fluid